X-Ray Imaging Methods: theory and applications

Maria Civita

April 2013

Contents

Chapter 1

X-Ray microscopy

1.1 Introduction to modern microscopy

Microscopes using visible light and a system of lenses to magnify images of small samples are convenient and ubiquitously used but they have limitations. In fact the resolution is generally limited by the wavelength of visible light to some 100-s of nanometers. Furthermore many materials are opaque to visible light, so there is need for better penetration and higher resolution.

Transmission Electron Microscopes (TEM) operate on the same basic principles as the light microscopes but use electrons instead of light. The source's much lower wavelength leads to a dramatic improvement in terms of resolution which makes it possible to see objects to the order of a few angstrom. One limitation of the TEM is that, unless the specimen is made very thin, electrons are strongly scattered within the specimen, or even absorbed rather than transmitted. This constraint has provided the incentive to develop electron microscopes that are capable of examining relatively thick (so called bulk) specimens.[1].

In the Scanning Electron Microscopes (SEM) the high-energy electron focused beam is used to scan the specimen. The signals that derive from electron-sample interactions are used to generate high-resolution images of shapes of objects and to show spatial variations in chemical compositions[2]. In most cases specimens to be analyzed are allocated in a proper vacuum chamber and must be electrically conductive, at least at the surface, and electrically grounded to prevent the accumulation of electrostatic charge at the surface. The image resolution, typically between 3 nm and 10 nm, is not as good as the TEM but much superior to the light microscope.

Another class of microscopes is characterized by a scanning probe where a sharply-pointed tip (the probe) is mechanically scanned in close proximity to the surface of a specimen in order to sense some local property. The first such device to achieve really high spatial resolution was the scanning tunneling microscope (STM)[3] in which a sharp conducting tip is brought within about 1 nm of the sample and a small potential difference

(circa 1 V) is applied. Another example of scanning probe microscope is given by the Atomic Force one (AFM) in which a sharp tip (at the end of a cantilever) is brought sufficiently close to the surface of a specimen, so that it essentially touches it and senses an interatomic force[4]. In both cases it is possible to achieve a very high resolution (0.1-0.5 nm) but the big limit to these microscopes is that the information comes from the surface, not from what lies below it.

In order to overcome this limitation X-ray microscopes have been developed. They are particularly powerful in imaging those samples whose structures are on length scales that are intermediate between those probed by optical and electron based techniques.

The following table presents a summary of what has been said so far, also including the nano-probe microscopes which will not be treated in this report.

Microscope Type	Detect	Resolution	Contrast
visible light	transmitted light	500 nm	bright field
		500 nm	phase contrast
	scattered light	500 nm	dark field
	fluorescence	50 – 500 nm	label
electron microscope (TEM)	scattered electrons	0.1 – 1 nm	heavy metal stain
scanning electron micr. (SEM)	secondary electrons	3 – 10 nm	surface relief
scanning tunneling micr. (STM)	tunneling current	0.1 nm	surface atoms
scanning force micr. (AFM)	force on probe tip	0.5 nm	surface relief
X-ray projection microscope	transmitted X-rays	>1000 nm	absorption
X-ray microscope (TXM)	transmitted X-rays	25 nm	absorption
		25 nm	phase contrast
scanning X-ray microscope (STXM)	transmitted X-rays	25 nm	absorption
			XANES (chemical)
nanoprobe	fluorescence	30 nm	elements
	diffraction	30 nm	strain

Figure 1.1: Overview table on modern microscopes adapted from the Xradia website.

1.2 X-ray microscopes

X-ray microscopy stands out from optical microscopy and electron microscopy due to its small working wave length (which means a higher Rayleigh resolution, compared with optical microscopy), and its large penetration distance and small radiation damage if compared with electron microscopy. The interaction of X rays with matter provides abundant information. Therefore X-ray microscopy has the capability to offer both spatial information and chemical/physical information, which makes it even more attractive. In the past three decades, modern X-ray microscopy has been well developed [5]. This is not only due to the availability

of high brightness synchrotron light sources and micro-fabricated high resolution X-ray optics, but also due to the dramatically increased needs from biological and material sciences.

Third generation synchrotrons are characterized by an high Brilliance, defined as the number of photons generated per unit time per unit source area (mm^2) per unit solid angle ($mrad^2$) per 0.1% fractional bandwidth ($\Delta\lambda/\lambda$), and by a sufficient coherent flux depending on the emittance of the circulating electron beam [6]. In the synchrotron, electrons circulate at high speed in vacuum within a storage ring where they not follow a purely circular orbit, but traverse through straight sections where lattices of magnets, or undulator insertion devices, force them to execute small-amplitude oscillations. At each oscillation X-rays are emitted and when the different contributions from the passage of a single electron add coherently, a very intense beam results. Another important component is the monochromator which permits to choose a wavelength bandwidth in accordance with what is needed for the experiment. Last but not least for importance, the focusing devices which are necessary to illuminate the sample and to achieve an high resolution.

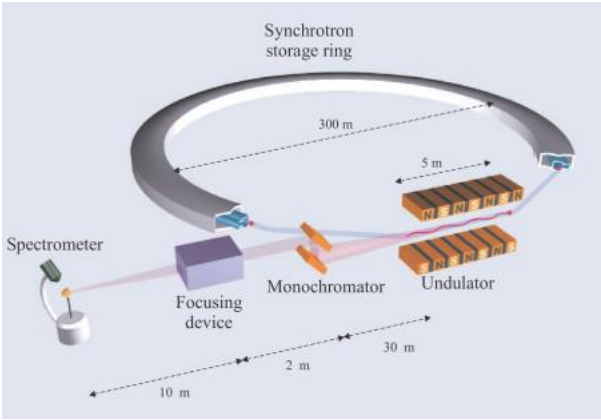

Figure 1.2: Schematic of a typical X-ray beamline at a third generation X-ray source. Figure extracted from [7].

1.2.1 Focusing devices

The first focusing devices developed for X-rays were the KB mirrors (owing their name to their inventors Kirkpatrick and Baez in 1948[8]). The system is based on two curved mirrors which are placed orthogonally with respect to each other and designed such that they both focus to the same point in space.

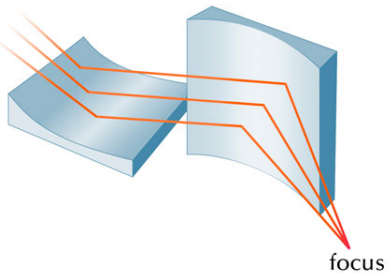

Figure 1.3: KB mirrors schematic adapted from the Xradia website.

The KB mirror system has endured to the present day and in fact we have used it during several experiments at the Advanced Photon Source facility.

Another class of lens based system comprehends Compound Refractive Lens (CRLs) [9] and Fresnel Zone Plates (FZP) which we have used several times during our experiments at APS, Elettra and Swiss Light Source.

A Fresnel zone plate typically consists of a plate with circular concentric ribs (See Fig. 1.4 a and b) and can be thought of as a circular diffraction grating.

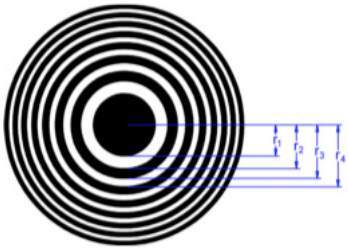

a)

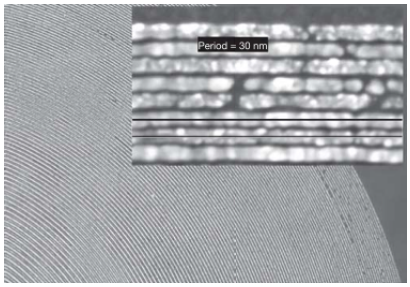

b)

Figure 1.4: a) Schematic representation of a FZP b) Scanning electron micrograph of a zone plate with 15 nm outermost zone [10].

The structure of a zone plate is made in such a way that the spacing between the peripheral rings becomes much smaller going to the edge of the plate itself. This is important because in this way the FZP works like a lens with different focal points. In fact the focal distance is related to the spacing between the rings by the formula

$$f_n = \frac{D^2}{4n\lambda} = \frac{Dd_n}{\lambda} \tag{1.1}$$

where D is the zone plate diameter and d_n is the spacing between two rings in a defined region of the FZP. For this reason, when fully illuminated, the zone plate presents several diffraction orders and it is possible to select one by using an Order Sorting Aperture (OSA) downstream of the beam. This will be better illustrated when talking about the Scanning Transmission X-ray Microscope (STXM).

1.2.2 Transmission X-ray Microscope

The first TXM was built at Gottingen University by the group of Günter Schmahl [11]. A representative layout is shown in Figure 1.5. It is similar to a regular optical microscope.

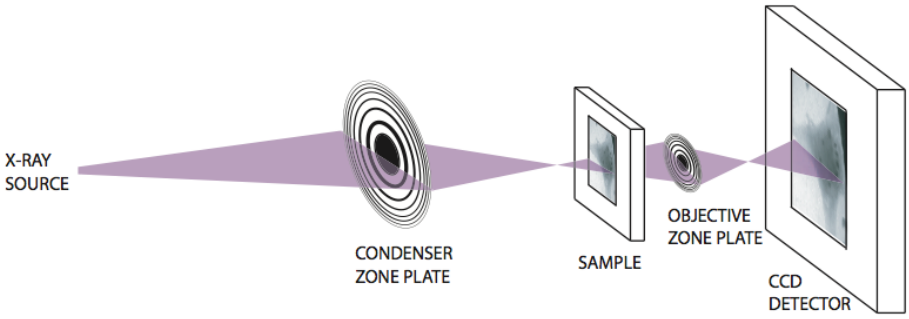

Figure 1.5: A full field transmission X-ray microscope (TXM) uses two zone plate lenses, condenser and objective, to form a 2D image on a spatially resolving detector. A pinhole order sorting aperture between condenser and the sample is not shown in the figure for the sake of clarity. Picture adapted from [12].

A large condenser zone plate, which has a large central stop, is used to illuminate the sample and a small high resolution "micro" zone plate is used as an objective lens to provide a magnified image to a two dimensional CCD detector. The condenser is not only used to deliver intense illumination, but some- times it also serves as a monochrometor to provide the required temporal coherence (because the objective is also a chromatic optic). A pinhole is inserted between the condenser and the sample to block the zero and high order diffraction from the condenser zone plate.

1.2.3 Scanning Transmission X-ray Microscope

A STXM works in a way similar to that of a Scanning Electron Microscope (SEM)[13]. The first STXM using a zone plate focused X-ray beam was built by the Stony Brook group at the National Synchrotron Light Source (NSLS) at Brookhaven National Laboratory. Figure 1.6 shows the configuration of a typical STXM.

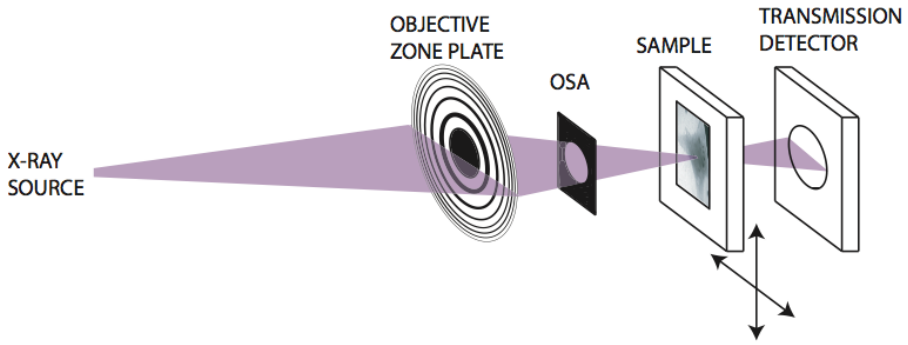

Figure 1.6: Scanning transmission X-ray microscopes (STXM) use a objective zone plate to focus the X-ray beam to a spot on a sample. The sample is then raster scanned through the focal spot and transmitted X-ray beam intensity is recorded on the detector for each scanned position. Picture adapted from [12].

A zone plate is illuminated by a near plane wave monochromatic X-ray beam, and focus the beam onto the sample. The transmitted X-ray flux is measured by a detector downstream of the sample. The sample, instead of the beam, is raster scanned by a stage driven by either piezoelectric positioners or stepping motors. Similar to the practice with condenser zone plates of TXMs, an order sorting aperture is important to filter the unwanted diffraction orders.

I first used a STXM to obtain quantitative phase contrast images during my experiment at the cSAXS beamline at the Swiss Light Source facility. The method that we applied is the Differential Phase-contrast (DPC) X-ray imaging that uses information concerning the phase gradient of an X-ray beam that passes through an object (whose refractive index is complex) in order to create its images[14]. In this case the phase gradient causes a redistribution of the intensity across the detector plane. The idea is then to use an anti-symmetric detector response function that will be sensitive to the redistribution of the intensity. In this experiment, which will be described in detail in Chapter 4, we were looking at gold nanocrystals deposited on a membrane.We firstly defined a region of interest around the crystal and then we calculated the differential phase contrast along both the x and y directions on the sample plane, as well as the integrated phase in the forward direction, where we had a PILATUS 2M detector at 7.2m downstream of the sample.

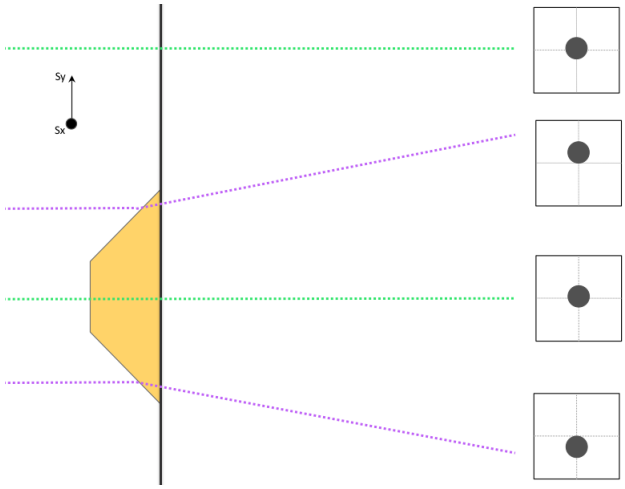

Figure 1.7: Phase contrast acquisition schematic.

The green dashed lines in Fig. 1.7 represent the beam when not touching the crystal or when hitting the crystal surface perpendicular to the beam itself. The result in these conditions was to observe a dark spot on the detector in the middle of our region of interest. If we moved the beam, for example along y (violet dashed lines in the figure), refraction occurred and as a result we saw our spot shifted along y. We then repeated the same procedure along x observing this time a shift of the spot on the left-right side. At this point we used a routine to evaluate the differential phase contrast in both directions by using the relation between the the angular deviation of the beam (dark spot) and the gradient of the phase as

$$DPC_x = \frac{\lambda}{2\pi}\frac{\partial\phi(x,y)}{\partial x} \tag{1.2}$$

$$DPC_y = \frac{\lambda}{2\pi}\frac{\partial\phi(x,y)}{\partial y}.$$

We then calculated the differential phase contrasts integrals to obtain the whole integrated phase which gave us information about the thickness of our crystal as well as the total phase shift, as described in Fig. 1.8.

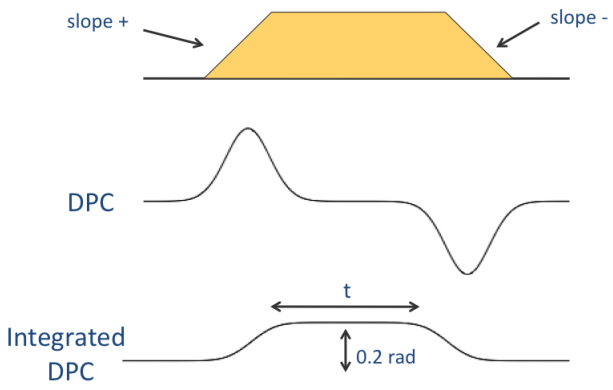

Figure 1.8: Differential phase contrast and integrated phase schematic.

The experimental results of the phase contrast analysis are showed in Fig. 1.9.

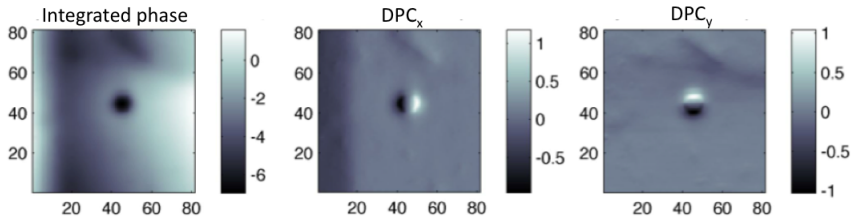

Figure 1.9: Phase Contrast analysis of a gold nanocrystal performed at the cSAXS beamline. The nanocrystal size is about 372x248nm^2(12pixel in horizontal and 8pixels in vertical, where the pixel size is around 31nm as calculated in Eq. 4.1).

1.2.4 Structured Illumination Microscopy

Structured illumination microscopy (SIM) is based on the concept of illuminating the sample with patterned light and it is used to gain a factor two improvement in the lateral resolution [15] as well as to achieve optical sectioning [15, 16, 17, 18, 19]. Last year I took part to an experiment based on structured illumination using X-rays at the TwinMic beamline at the Elettra synchrotron in Trieste. The TwinMic X-ray spectromicroscope combines full-field imaging (TXM) with scanning X-ray microscope (STXM) in a single instrument. The idea of the experiment was to generate an incoherent structured illumination by imaging a transmission grating on to the sample using a condenser zone plate. We made a distinction between the illumination system, upstream of the sample, which made use the STXM part of TwinMic and the TXM part, downstream of the sample. A schematic representation of the experiment is showed in Fig. 1.10.

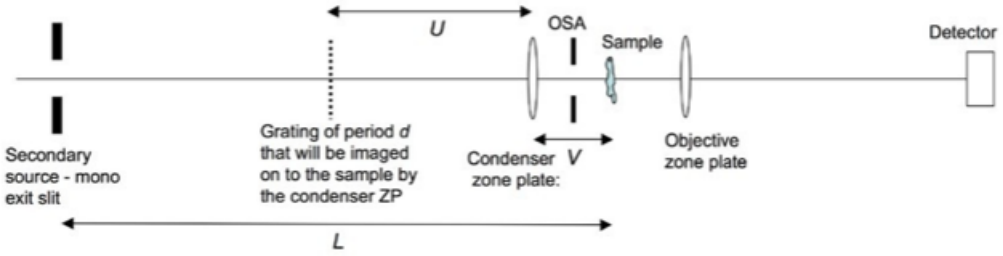

Figure 1.10: Structured illumination experiment at TwinMic.

The sample we used consisted of an etched pattern in a thin tungsten layer on a silicon nitride window. After illuminating the sample we recorded TXM images for a series of transverse shifts of the grating. Each shift moved the grating by a certain portion of a period (for instance one quarter of a period) in the manner of a phase-stepping interferometer [20] so to introduce a phase shift between the intensity functions of the sample and the grating. We then wanted to recover images of each sample section by operating a Fourier transform of the data with respect to the phase-shift variable. To demonstrate optical sectioning we needed to repeat the same procedure described above for a series of positions on and off focus. Successful sectioning would have returned a good image along an in-focus strip and darkness elsewhere. The aim of this proposal was to both achieve optical sectioning of our sample as well as increasing the resolution, but we could not succeed due to technical difficulties. For this reason we have re-applied our proposal to TwinMic and plan to repeat the experiment in May this year.

Chapter 2

Coherent X-ray Diffraction Imaging

Coherent X-ray diffraction imaging (CXDI) is a technique where an highly coherent beam of X-rays is used to resolve the structure of nanoscale samples such as nanotubes[21], nanocrystals[22] and more. The main advantage of CDI is that it does not use lenses to focus the beam so that the measurements are not affected by aberrations and the resolution is only limited by diffraction and dose. In a typical CDI experiment, the coherent beam produced by a synchrotron source is scattered by the sample so that to generate diffraction patterns which are collected downstream by a detector. The recorded data is described in terms of absolute counts of photons, a measurement which describes amplitudes but loses phase information. In order to retrieve the image of the sample in both its amplitude and phase it is then necessary to solve what is commonly called the "phase problem".

2.1 The phase problem in CXDI

In CXDI diffraction patterns are collected in the far field, or Fraunhofer region, meaning that the distance between the sample and the detector must be $D > a^2/\lambda$ being a the illuminated sample size and λ the radiation wavelength. In this region the diffracted wave is given by the Fourier transform of the wave exiting from the sample

$$F(\mathbf{q}) = \int \varrho(\mathbf{r}) e^{i\mathbf{q}\cdot\mathbf{r}} d^3\mathbf{r} \tag{2.1}$$

where $\mathbf{q}$ is the scattering vector and $\mathbf{r}$ is the real space vector. The $\mathbf{q}$ vector is obtained by the subtraction of the incoming and diffracted wavevectors, $\mathbf{q} = \mathbf{k} - \mathbf{k}'$, and it can also be related to the detector distance as showed in Fig. 2.1.

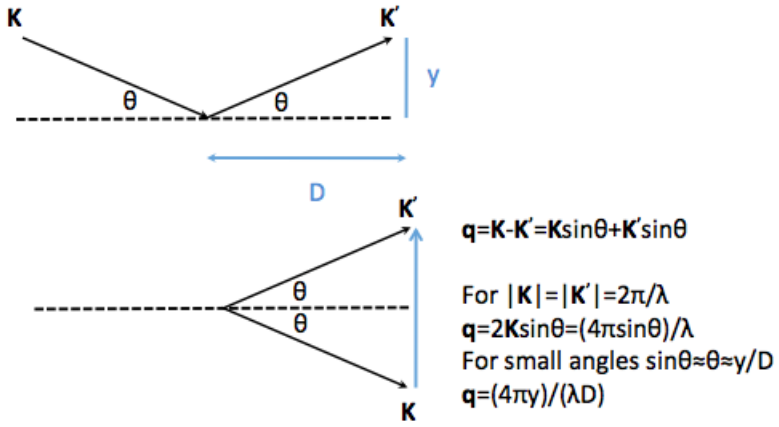

Figure 2.1: Schematic representation for calculating the scattering vector. An incoming beam of wavevector $\mathbf{k}$ hits a surface at a certain angle θ and is scattered along the $\mathbf{k}^{'}$ direction. Because $\mathbf{q}$ is by definition given by $\mathbf{q} = \mathbf{k} - \mathbf{k}^{'}$, in the case the two wavevectors are equal in modulus it is possible to say that $\mathbf{q} = 2\mathbf{k}sin\theta$. Being D the distance to the detector and y the point in which k' hits the detector (whose numerical size can be evaluated by the pixel size multiplied by the pixel number in position y), it is possible to write $\mathbf{q} = \frac{4\pi y}{\lambda D}$, in the case that θ is small enough so that $sin\theta \approx \theta \approx$y/D.

The exit wave is the complex function $\rho(\mathbf{r})$ which encloses the information about the electron density of the scattering object. It would seem straightforward that in order to retrieve all information about the sample it would be enough to just perform the inverse Fourier transform of the diffracted wave

$$\rho(\mathbf{r}) = \mathcal{F}^{-1}[F(\mathbf{q})]. \tag{2.2}$$

The problem with what stated above is that what is collected on the detector is proportional to the intensity of the diffracted wave

$$I(\mathbf{q}) = |F(\mathbf{q})|^2 \tag{2.3}$$

and so all the information about the phase of the complex function $F(\mathbf{q})$ is lost. Always keeping in mind the properties of Fourier transforms it is possible to relate the Fourier transform of the recorded intensity to the autocorrelation function of the electron density $\rho(\mathbf{r})$

$$|F(\mathbf{q})|^2 = \rho(\mathbf{r}) \otimes \rho(-\mathbf{r}) = g(\mathbf{r}) \tag{2.4}$$

that is a non-zero function twice the size of $\rho(\mathbf{r})$. The sample phase needs to be recovered in other ways and

what we usually do is to use iterative inversion algorithms with the aim of recovering the phase starting from a guess which is refined step by step.

2.2 Phase retrieval methods

As stated above, phase retrieval can be described as the task of obtaining the phase of the Fourier transform of a function (image) when only the magnitude (modulus) of this Fourier transform is known. Because an inversion method is used, starting from the the recorded intensity, it is important to establish whether the obtained solution is unique or not. In 1982, using the argument that the autocorrelation function of any sort of image is twice the size of the image itself in each dimension (as showed in the previous paragraph), Bates [23] stated that the phase information could be recovered by oversampling the magnitude of a Fourier transform that is twice as fine as the Bragg density (2X oversampling in each dimension: 4X for two dimensions and 8X for three dimensions). In this way he showed that for 2D and 3D problems there is almost always a unique solution to the phase problem.

2.2.1 Oversampling

The sampling theorem, mainly known as the Nyquist-Shannon theory, states that a band-limited function can be perfectly reconstructed from an infinite sequence of samples if the band-limit, B, is no greater than 1/2 the sampling rate (samples per second). This can be easily understood if we consider that sampling basically means to extract a series of values from a function, and this can be seen as multiplying the varying function by a Dirac comb.

$$f(x) * \sum_{k=-\infty}^{\infty} \delta(x - kT) \tag{2.5}$$

If we move this to the frequency domain, the multiplication by a Dirac comb results as a convolution by the Fourier transform of the comb, which is still a comb, whose effect is to replicate the function's spectrum at different frequencies.

$$F_s(s) = F(s) \otimes \frac{\sqrt{2\pi}}{T} \sum_{k=-\infty}^{\infty} \delta(s - k\frac{2\pi}{T}) \tag{2.6}$$

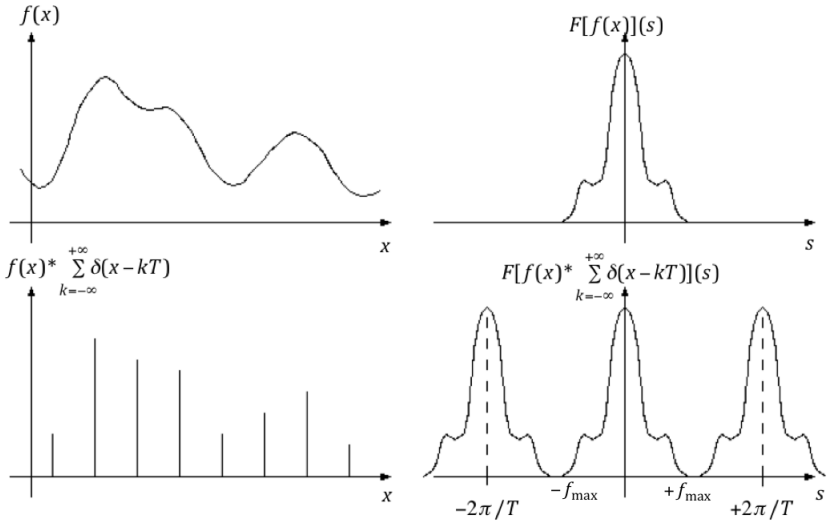

Figure 2.2: Function f(x) is showed in both space and frequency domains (left-right) in both unsampling (up) and sampling (down) conditions. Adapted from [24].

It can be easily understood from Fig.2.1 that if the sampling condition

$$f_s \geqq 2f_{max} \tag{2.7}$$

is not respected then all spectrums will overlap and aliasing will take place.

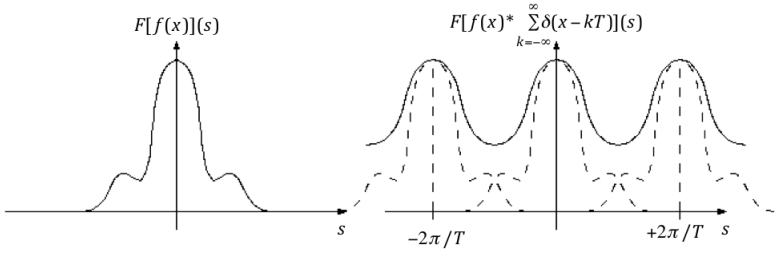

Figure 2.3: Effect of wrong sampling in the frequency domain. Adapted from [24].

Moving to our main problem, that is what to do with our diffraction intensities, we can say that given the exit wave $\rho(\mathbf{r})$, its Fourier transform $F(\mathbf{q})$ is given by

$$F(\mathbf{q}) = \int_{-\infty}^{\infty} \rho(\mathbf{r}) e^{2\pi i \mathbf{q}\cdot\mathbf{r}} d\mathbf{r} \tag{2.8}$$

where r_i are the spatial coordinates in image space and q_i are the spatial-frequency coordinates in Fourier space. Adopting this notation is convenient because what we collect is discretized in pixel units, so we need to approximate the object and its Fourier transform by arrays. If we now apply a conventional sampling and consider the discretized Fourier transform of the object function, we get

$$|F(\mathbf{q})| = \left| \sum_{\mathbf{r}=0}^{N-1} \rho(\mathbf{r}) e^{2\pi i \mathbf{q}\cdot\mathbf{r}/\mathbf{N}} \right| \tag{2.9}$$

where N is the number of pixels (from 0 to N-1 in each direction). Equation 2.9 is, according to Miao [25], actually a set of equations and the phase problem solution leads to solving $\rho(\mathbf{r})$ for each element of the array (or pixel). Finding a solution for this set of equations is not easy. First of all, due to the loss of phase there can be some ambiguities such as not being able to distinguish between these quantities: $\rho(\mathbf{r})$, $\rho(\mathbf{r}+\mathbf{r}_0)e^{i\theta_c}$ and $\rho^*(-\mathbf{r}+\mathbf{r}_0)e^{i\theta_c}$ where $\mathbf{r_0}$ and θ_c are real constants. If we concentrate on other nontrivial solutions we can distinguish between two cases. The first is to consider $\rho(\mathbf{r})$ complex and this means having, for the 1D problem, N equations to solve and 2N unknown variables (phase and amplitude for each pixel). This happens for the 2D and 3D cases where we have $N^2$and N^3equations and $2N^2$and $2N^3$variables, respectively. If we instead consider $\rho(\mathbf{r})$ to be real and we take the central symmetry of diffraction patterns into account (Friedel's law), the equation number in the system drops by a factor of 2, as well as the number of unknown variables. Still we have a problem which is underdetermined (number of equations $<$ number of unknown variables) by a factor of 2 for all dimensions. At this point it is clear that in order to solve equation 2.9 we need to have some a priori information about our sample and we need to introduce some constraint in our set of equations if we want to retrieve the phase. Miao thought about two main strategies to solve this problem. The first strategy consists on decreasing the number of unknown variables by using objects with some known scattering density (some known-valued pixels) inside them. For example one could use a sample with some non scattering density inside it. In this case it is possible to consider the ratio σ

$$\sigma = \frac{total - number - pixels}{not - known - pixels} \tag{2.10}$$

being the not known pixels the number of variables to be solved. To solve the system of equations it would be enough to have $\sigma > 2$. One could argue that being the number of unknown variables equal to the number of equations is a necessary, but not sufficient, condition for finding a solution for Eq. 2.9. Miao states that in these conditions this should not be a problem, referring to Barakat and Newsam's work on phase recovery[26], as well as to the important roles played by the positivity constraints[1] . Another strategy to solve Eq. 2.9 is to use the oversampling method. The idea is to oversample the magnitude of the Fourier transform to make

[1]In the case of x-ray diffraction, the complex-valued object density can be expressed by using the complex atomic scattering factor,$f1 + if2$ where f1 is the effective number of electrons that diffract the photons in phase (usually positive for x-ray diffraction), and f2 represents the attenuation, that is always positive for ordinary matter. The statement that f1 is usually positive and f2 is always positive is rigorously verified in experiments and for this reason it it possible to say that the object is positive, even for complex samples [25].

the ratio $\sigma > 2$. Extending this to two and three dimensions it is necessary to have $\sigma > 2^{1/2}$ and $\sigma > 2^{1/3}$ respectively.

2.2.2 Iterative algorithms

All iterative phase retrieval algorithms are based on the idea of assigning a phase to the diffraction intensities and refining this value at each iteration. In order to converge to a solution it is necessary to provide some constraints, related to a priori information about the sample or the experimental method. The general scheme of these algorithms is showed in Fig. 2.4.

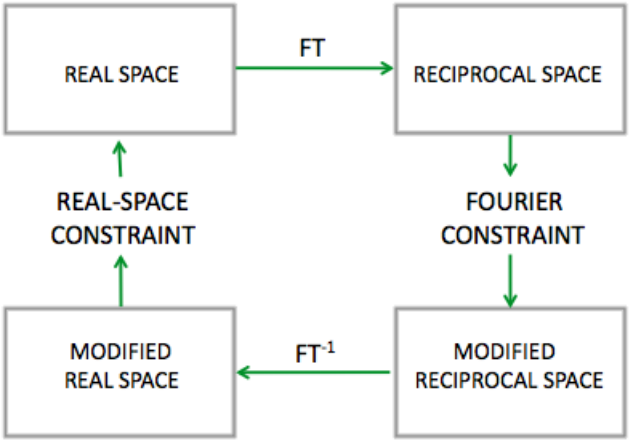

Figure 2.4: Phase retrieval iterative algorithm schematic.

If the iterative procedure gets to convergency, the now phased diffraction can be inverted to obtain the whole object reconstruction in both phase and amplitude.

The starting point of these algorithms is to define a guess of the object in the real space $\rho(r)_c$ which is then transformed, using the discrete fast Fourier transform (FFT). The resulting complex quantity is then compared with the experimental data. The computed amplitudes are then replaced with the experimental ones while the phase is kept, following the formula

$$F(\boldsymbol{q})' = \frac{F(\boldsymbol{q})}{|F(\boldsymbol{q})|}\sqrt{I(\mathbf{q}_{measured})} \tag{2.11}$$

which is commonly called the Fourier constraint. What is obtained after applying Eq. 2.11 it then converted to the real space by using an inverse Fourier transform. It is at this point that real space constraints are applied to get the updated object function $\rho(r)_{c+1}$. This procedure is repeated iteratively until getting to a convergency condition.

There are several algorithms which are used to retrieve the phase and here I will talk about the two that are mostly used: the Error Reduction (ER) and the Hybrid Input-Output (HIO) [27]. Both of them start with the definition of a region of space where the object is defined, the support, and it is assumed that the real space outside this region has zero amplitude for all the iterative transformations. In order to make such an assumption it is necessary to have some a priori knowledge of the sample or to derive it from the autocorrelation function of the object function (see Eq. 2.4).

The ER algorithm is directly descendant from what stated above and it consists on updating the object function in such a way that the object is always forced to only exist within the support S, whereas it is set to zero outside.

$$g_{c+1}(\boldsymbol{r}) = \begin{cases} g'_c(\boldsymbol{r}) & \text{if } \boldsymbol{r} \in S \\ 0 & \text{if } \boldsymbol{r} \notin S \end{cases} \tag{2.12}$$

This algorithm minimizes the distance between the distance between the real and Fourier space constraints at each iteration and when a local minima is reached the object function is no longer updated[27]. This can be a problem since the stagnation in the local minima condition may lead to a wrong solution.

In order to solve this problem the HIO algorithm updates the object function by using together the outputs of the current and previous iterations (c^{th} and $c-1^{th}$), controlled by a feedback parameter β whose value is usually chosen between 0 and 1.

$$g_{c+1}(\boldsymbol{r}) = \begin{cases} g'_c(\boldsymbol{r}) & \text{if } \boldsymbol{r} \in S \\ g_c(\boldsymbol{r}) - \beta g'_c(\boldsymbol{r}) & \text{if } \boldsymbol{r} \notin S \end{cases} \tag{2.13}$$

The two algorithms are also used together, for example the iterations start with the HIO to look for a solution and then there is a switch to the ER to converge to a local minimum. In this case and under certain conditions, stagnation may still occur [28].

2.3 Coherence of X-Ray sources

The theoretical treatment discussed in the previous paragraphs relies on the coherence of the beam. Optical coherence occurs if, considering a given radiating region, the phase differences between all pairs of points have definite values which are constant with time. The resulting sign of high coherence is the ability to form interference fringes of good contrast [29].

There are two types of coherence that need to be specified: the longitudinal and transverse ones. An example of radiating region with longitudinally and transversely coupled points is showed below in Fig. 2.4.

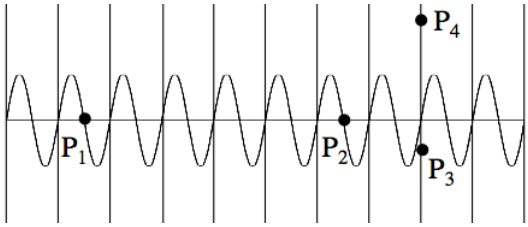

Figure 2.5: Radiating region with a couple of longitudinally separated points (P1-P2) and transversely separated points (P3-P4). Figure adapted from [29].

The longitudinal coherence length can be defined by considering two wavefronts with different wavelength which start off in phase and travel in the same direction. The distance the two wavefronts cover before going back to being in phase is defined as twice the longitudinal coherence length ($2L_{L)}$, while when they are out of phase by a factor of π the distance is only L_L.

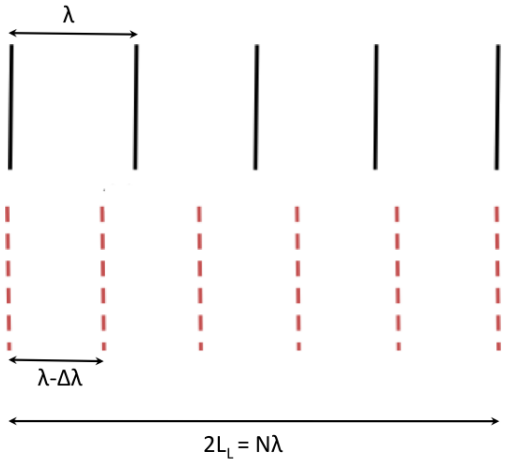

Figure 2.6: Example to show how to calculate the longitudinal coherence length L_L. Figure adapted from reference [7].

If we assume that $2L_L$ is equal to a multiple N of wavelengths, then it is easy to calculate the longitudinal coherence length as a function of λ

$$L_L = \frac{\lambda^2}{2\Delta\lambda}. \tag{2.14}$$

The transverse coherence length is related to the collimation of the beam, in fact in order to define it we consider two waves with the same λ emitted from a source of a finite size D.

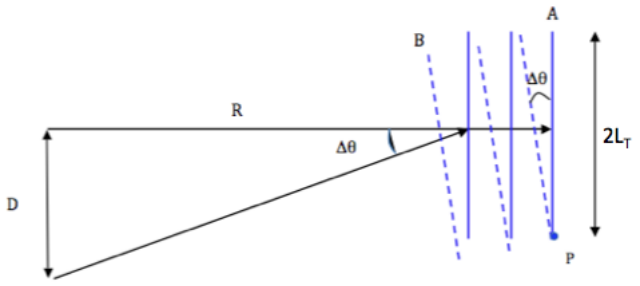

Figure 2.7: Example to show how to calculate the longitudinal coherence length. Figure adapted from [7].

In this case the two wavefronts (A and B in the figure) only differ in their propagation directions by a small amount defined by the angle $\Delta\vartheta$. At point P the wavefronts coincide and the transverse coherence length L_T is defined as the distance along A in which the two waves are out of phase. Again as for the longitudinal case, if proceeding to a distance of $2L_T$the two waves go back to being on phase. From Figure 2.7 it is easy to observe that $\lambda = 2L_T\Delta\vartheta$ where the angle $\Delta\vartheta$ can also be defined as $\Delta\vartheta = R/D$, so in the end we get

$$L_T = \frac{\lambda}{2\Delta\vartheta} = \frac{\lambda R}{2D}. \tag{2.15}$$

In synchrotrons sources the beam obtained by the circulating flux of electrons has a Gaussian shape and its coherence is defined by the undulators. In this case we define horizontal and vertical transverse coherence lengths as

$$L_{TH} = \frac{\lambda R}{2\pi\sigma_H},\ L_{TV} = \frac{\lambda R}{2\pi\sigma_V} \tag{2.16}$$

where σ_H and σ_V are the horizontal and vertical sizes of the beam, respectively. The transverse coherence can be improved thanks to the use of slits in the beamline.

The longitudinal coherence obtained in a synchrotron is related to the bandwidth of the optics used in the beamline. The most influent component is the monochromator and the optical path length difference (OPLD) between two different parts of the beam traveling in it, is defined as the longitudinal coherence of the beam. If the OPLD is smaller than the L_T the beam is in the coherent limit.

Chapter 3

Ptychography

Ptychography is an imaging method which can be considered as a development of the classical CXDI described in the previous chapter. The first inventors of Ptychography were Hegerl and Hoppe in 1970 [30], who also named it starting from the greek word 'ptycho', which means 'to fold', to describe that at the basis of this method there is a convolution operation between two functions (that is two functions folding together in mathematical terms). It was clear from the beginning that Ptychography was a useful tool to solve the phase problem, but the limits in the computing power in the early 70s did not allow a real application. For this reason it was only in the past decade that this powerful tool has been further developed and used as an imaging method. The pioneer in the field was John Rodenburg who proved in the late 90s the effectiveness of this method and provided the first inversion algorithm [31, 32, 33, 34, 35]. In recent years Ptychography has been used in many fields, from imaging computer chips [36]to biological samples [37, 38, 39]. The new frontier is to remove the requirement of coherence in the beam [40], this to say that this method is constantly growing.

3.1 Theoretical principles of Ptychography

The idea at the basis of Ptychography is to use an highly focused and coherent beam, the probe, to scan an extended object at different positions and to then collect the resulting diffraction patterns in the far field. This is a big difference from the CXDI described in Chapter 2 because in that case there was only one diffraction pattern, while now the dataset is composed by a number of recorded diffraction patterns, one for each probe position. The scanning probe must move onto the sample in such a way that there is always an overlap region between two contiguous illuminating positions. This causes a redundancy in the dataset which helps to retrieve the phase of the object without the requirements to oversample the diffraction patterns in the Fourier plane and to have a sample of finite extent within the coherent beam.

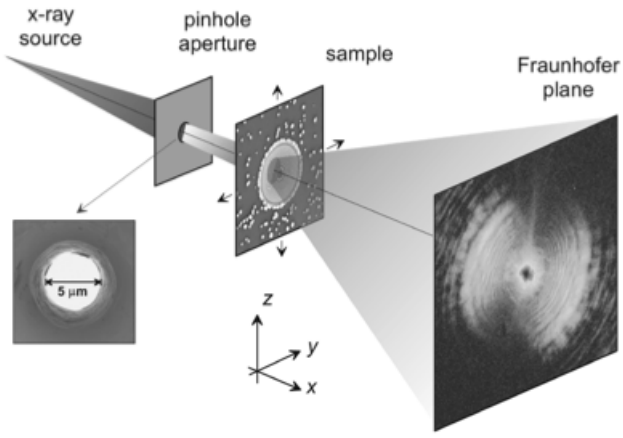

Figure 3.1: Schematic representation of the setup used by Rodenburg in 2007, extracted from his publication [33]. In this case the beam is focused with a pinhole and the sample is mounted on a 2D piezo stage which moves on the yz plane. For each probe position a diffraction pattern is recorded by a CCD camera at the Fraunhofer plane (far field).

This method has proved to be successful not only in the X-Rays regime, but also at optical [41] and electron microscopy [42] wavelengths.

The phase problem is solved with the aid of iterative inversion algorithms which transform and update functions back and forth between the real and Fourier spaces. What is different from what described in the previous chapter is that the redundancy in the collected data is used to update the object function in the real space, so that there is no requirement for a real space constraint (defined region of space where the real object exists).

There are many algorithms to process this kind of inversion, and this is something which will be briefly discussed in the last chapter of this report, but here I will describe the most robust and famous ones: PIE, ePIE and the Difference Maps algorithms.

3.2 Ptychographic Iterative Engine (PIE)

The PIE algorithm was the first one to be implemented by Rodenburg [43] and it assumes, as well as all the following methods do, a multiplicative relationship between the object and probe complex wave-functions to create the exit-wave

$$\psi(\mathbf{R}) = O(\mathbf{R})P(\mathbf{R}) \tag{3.1}$$

being $O(\mathbf{R})$ the object function and $P(\mathbf{R})$ the probe or illumination function. Rodenburg pointed out in his paper that this relation is generally accurate for thin objects. It is also assumed that $O(\mathbf{R})$ or $P(\mathbf{R})$ can

be moved relative to one another by various distances **R**. In the following description it will be considered the case of the probe moving with respect to the object, but the result would not be different if moving the object function instead. In order to use this method it is necessary to know all the illumination functions as well as all the scan positions, and of course all the diffracted intensities collected in the far field.

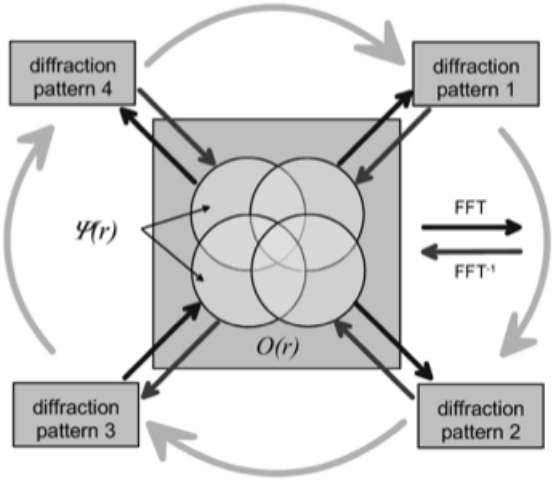

Figure 3.2: Schematic representation of how the PIE algorithm works on four overlapping probe positions (circles) illuminating a region of an extended object (central square). Figure obtained by [33].

The whole method can be described by several steps.

1. The algorithm starts with a guessed (g) object function in the real space $O_{g,n}(\mathbf{r})$ at the nth iteration.
2. It is the necessary to multiply the current guessed object function by the illumination function $P(\mathbf{r}-\mathbf{R})$ at the current position $\mathbf{R}$, so to produce a new guessed exit wave function

$$\psi_{g,n}(\mathbf{R}) = O_{g,n}(\mathbf{R})P(\mathbf{r}-\mathbf{R}). \tag{3.2}$$

3. The guessed exit wave is then Fourier transformed to obtain the corresponding function in the diffraction space, indicated by the reciprocal space coordinate $\mathbf{k}$.

$$\boldsymbol{\psi}_{g,n}(\mathbf{k},\mathbf{R}) = \mathscr{F}[\psi_{g,n}(\mathbf{R})] = \left|\boldsymbol{\psi}_{g,n}(\mathbf{k},\mathbf{R})\right| e^{i\theta_{g,n}(\mathbf{k},\mathbf{R})}. \tag{3.3}$$

It is worth noticing that this function is a guessed version of the diffracted exit wave, since it is obtained starting from a guessed object function in the real space. Because the transformed exit wave is complex, it can be decomposed in both amplitude and phase.

4. Being the dataset composed by a series of diffracted intensities, it is now possible to replace the guessed

amplitude of the transformed exit wave with the recorded one

$$\boldsymbol{\psi}_{c,n}(\mathbf{k},\mathbf{R}) = |\boldsymbol{\psi}(\mathbf{k},\mathbf{R})|\, e^{i\theta_{g,n}(\mathbf{k},\mathbf{R})} \tag{3.4}$$

where $|\boldsymbol{\psi}(\mathbf{k},\mathbf{R})|$ is the modulus of the diffracted intensity.
5. At this point it is possible to inverse transform the modified exit wave, so to obtain a new improved guess in the real space

$$\psi_{c,n}(\mathbf{k},\mathbf{R}) = \mathscr{F}^{-1}\left|\boldsymbol{\psi}_{c,n}(\mathbf{k},\mathbf{R})\right|. \tag{3.5}$$

6. The guessed object function in the real space is then updated by

$$O_{g+1,n}(\mathbf{R}) = O_{g,n}(\mathbf{R}) + \frac{|P(\mathbf{r}-\mathbf{R})|}{|P_{max}(\mathbf{r}-\mathbf{R})|}\frac{P^*(\mathbf{r}-\mathbf{R})}{\left(|P(\mathbf{r}-\mathbf{R})|^2+\alpha\right)} \times \beta\left(\psi_{c,n}(\mathbf{k},\mathbf{R}) - \psi_{g,n}(\mathbf{k},\mathbf{R})\right) \tag{3.6}$$

where α and β are opportune parameters and $|P_{max}(\mathbf{r}-\mathbf{R})|$ is the maximum value of the illumination function. The value α is used to prevent a divide-by-zero occurring in the case that the modulus of the probe function is zero. The constant β controls the amount of feedback in the algorithm, and may be varied between roughly 0.5 and 1. Lower values of increase the importance of the newest estimate of the object function, whereas higher values increase the importance of the previous estimate.
7. The algorithm continues by moving to a contiguous position, for which there is an overlapping illumination region with the previous one.
8. All steps from 2 to 7 are repeated until the sum squared error (SSE) is sufficiently small

$$SSE = \frac{\left(|\psi(\mathbf{k},\mathbf{R})|^2 - |\psi_{g,n}(\mathbf{k},\mathbf{R})|^2\right)^2}{N}, \tag{3.7}$$

where N is the number f pixels in the array representing the wave function.

This algorithm works in a similar way to other iterative phase retrieval algorithms. For the case where $\beta = 1$ and $\alpha = 0$, and the function $|P(\mathbf{r}-\mathbf{R})|$ is a mask, or support function, the algorithm is very similar to the well-known Fienup algorithm [27].

3.3 Extended Ptychographic Iterative Engine (ePIE)

The PIE algorithm has been extended so that the requirement for an accurate model of the illumination function could be removed [44].

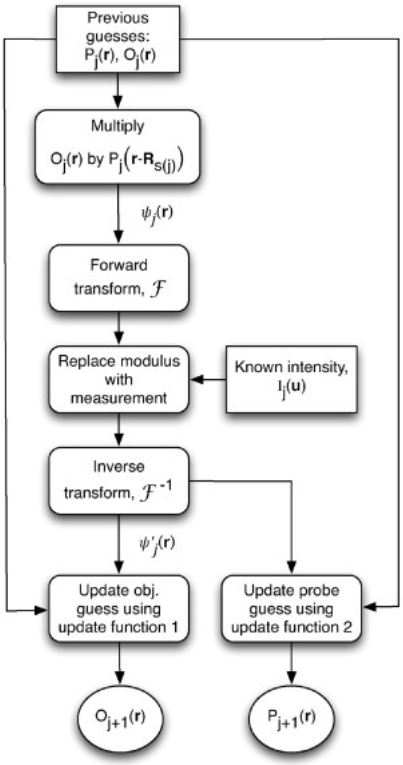

Figure 3.3: Flowchart of the ePIE method. At j=0 initial guesses at both the sample and probe waveforms are provided to the algorithm. Figure extracted from [44].

For this new version of the algorithm it is necessary to have initial guesses for both the object and probe wave-functions, labelled $O_0(\mathbf{r})$ and $P_0(\mathbf{r})$ respectively. Generally the initial object guess is taken as free-space, while the initial probe waveform is taken as a support function roughly the size of the intense region of the probe wavefront. Each diffraction pattern then is considered in turn, with the update of both the object and probe guesses at each step. This new approach leads to a much quicker rate of convergence.

If compared with the PIE method, this new extended version consists on following the steps described above, with the exception of the sixth one, where is a significant change in the use of update function, which is modified and applied to both object and probe functions.

$$O_{g+1,n}(\mathbf{R}) = O_{g,n}(\mathbf{R}) + \frac{P^*_{g,n}(\mathbf{r}-\mathbf{R})}{|P_{g,n}(\mathbf{r}-\mathbf{R})|^2_{max}} \times \beta \left(\psi_{c,n}(\mathbf{k},\mathbf{R}) - \psi_{g,n}(\mathbf{k},\mathbf{R})\right) \tag{3.8}$$

$$P_{g+1,n}(\mathbf{R}) = P_{g,n}(\mathbf{R}) + \frac{O^*_{g,n}(\mathbf{r}-\mathbf{R})}{|O_{g,n}(\mathbf{r}-\mathbf{R})|^2_{max}} \times \alpha \left(\psi_{c,n}(\mathbf{k},\mathbf{R}) - \psi_{g,n}(\mathbf{k},\mathbf{R})\right). \tag{3.9}$$

3.4 Difference Map method

The Difference Map method was initially defined by Elser in 2003 [45] and then widely adopted by Thibault for Ptychography [46, 47]. The kind of problems solved by the DM algorithm can be expressed as the search for the intersection point between two constraint sets. The exit waves ψ_j ("views" on the specimen) definition helps to relate the two intersecting constraints.

The Fourier constraint which relates the calculated amplitudes to the measured intensities can be written as

$$I_j = \left|\mathscr{F}\left(\psi_j\right)\right|^2, \tag{3.10}$$

while the Overlap constraint states that each view can be factorized as a probe and an object function:

$$\psi_j(\mathbf{r}) = O(\mathbf{r})P(\mathbf{r}-\mathbf{r_j}). \tag{3.11}$$

As it was for the PIE and ePIE algorithm, this method is based on several steps.

1. At the beginning it is necessary to produce an initial guess for the illumination function $P(\mathbf{r})$ and construct an initial state vector $,\boldsymbol{\psi} = \{\psi_1\left(\mathbf{r}\right), \psi_2\left(\mathbf{r}\right), ..., \psi_N\left(\mathbf{r}\right)\}$, being N the number of probe positions, formed following Eq. 3.11.
2. The method goes on with the update of both object and illumination functions

$$O_g\left(\mathbf{r}\right) = \frac{\sum_j P_g^*(\mathbf{r}-\mathbf{r_j})\psi_j\left(\mathbf{r}\right)}{\sum_j \left|P_g(\mathbf{r}-\mathbf{r_j})\right|^2} \tag{3.12}$$

$$P_g\left(\mathbf{r}\right) = \frac{\sum_j O_g^*(\mathbf{r}+\mathbf{r_j})\psi_j\left(\mathbf{r}+\mathbf{r_j}\right)}{\sum_j \left|O_g(\mathbf{r}-\mathbf{r_j})\right|^2} \tag{3.13}$$

using a small number of alternate applications of equations 3.12 and 3.13 and thresholding the guessed object function$O_g\left(\mathbf{r}\right)$ to maintain all amplitudes smaller than 1.

3. Arrived at this point all views contained in state vector are also updated by using the difference map update function

$$\psi_{j,n+1} = \psi_{j,n}\left(\mathbf{r}\right) + p_F\left(2P_g\left(\mathbf{r}-\mathbf{r_j}\right)O_g\left(\mathbf{r}\right) - \psi_{j,n}(\mathbf{r})\right) - P_g\left(\mathbf{r}-\mathbf{r_j}\right)O_g\left(\mathbf{r}\right) \tag{3.14}$$

where p_F the projection of each views onto the Fourier space constraint set, obtained by replacing the calculated amplitudes with the corresponding experimental diffraction intensities, while keeping the computed phase values.
4. The previous 2 and 3 steps are iterated until convergency is reached

$$Error_{n+1} = \left\|\psi_{n+1} - \psi_n\right\|.^2 \tag{3.15}$$

There are few big differences between the Difference Map method and ePIE. One is that the former is a parallel method which updates the object and probe functions simultaneously for the entire set of views, so that also the Fourier projection p_F can be calculated in a parallel fashion. This does not happen in ePIE, where all updates and projections are calculated serially. Another difference is in the update of the state vector, which is easier in ePIE and more complex in the DM method.

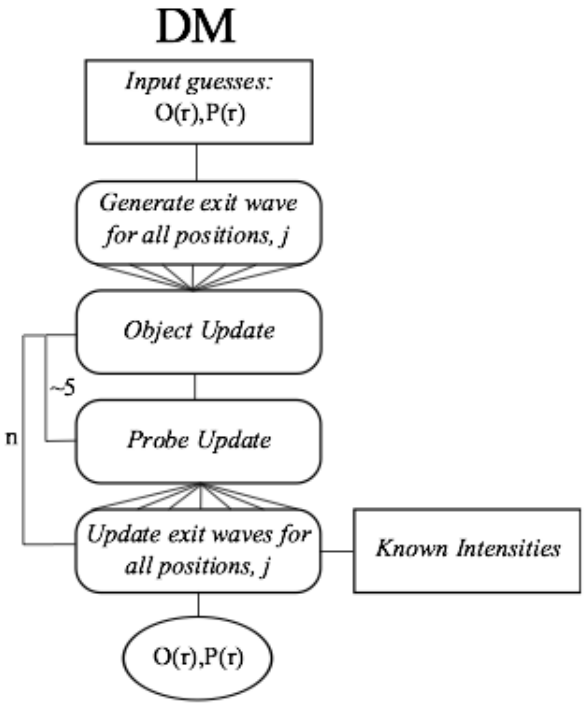

Figure 3.4: Difference Map algorithm flow-chart from [6].

Chapter 4

Experimental results

4.1 Ptychography on gold nanocrystals

Gold nanocrystals have been the subject of study of the UCL group for a number of years. The aim of this experiment was to use ptychography to collect diffraction patterns in the transmission geometry, when rocking the sample at different angles around the Bragg condition. We also used a second detector at the Bragg angle, in reflection geometry, with the aim of collecting the reflected intensities to then retrieve the experimental rocking curve. As a result we could measure a phase shift inside the crystals between the different rocking conditions. By comparing our results with those ones suggested by the theory, we managed to give a physical explanation to this remarkable effect. In this chapter I will try to give an explanation which only relates to the kinematical diffraction theory since we believe that gold nanocrystals might not be thick enough to take the dynamical theory into account. At present we are planning to repeat this experiment with another set of samples which we consider more suitable to investigate the dynamical regime (this will be better explained in the next chapter), but we are also collaborating with experts in the field with the aim to relate this result on gold nanocrystals to a dynamical effect.

4.1.1 Experimental setup

The experiment was conducted at the coherent small angle X-ray scattering (cSAXS) beamline at the Swiss Light Source, Paul Scherrer Institut. The experimental setup is showed in Fig. 4.1 and was composed of several components precisely aligned with the aid of the 'X-ray' eye system used at the cSAXS beamline. A similar setup is described on [48]. We illuminated the sample with a fully coherent beam at the energy of $8.7KeV$. To focus the beam we used a 30μm central stop and then a 75μm Fresnel Zone Plate with $100nm$

spacing between the concentric rings, in the outermost zone, and 1μm thickness, made of gold[1]. Downstream of the FZP we used a 20μm pinhole serving as order selecting aperture (OSA) to select the first diffraction order at a distance of $51mm$ from the FZP. The focal length of the zone plate was $52.66mm$ at the energy of $8.7KeV$. The sample was mounted on a high-precision piezoelectric positioning stage for high-resolution scanning downstream at $9.5mm$ from the OSA. We also used two PILATUS detectors with $172x172\mu m^2$ pixel having 20-bit dynamic range, no readout noise, and a point spread function of one single pixel. The PILATUS 2M detector sampled the far-field intensity with 1475×1679 pixels and was located at a distance of $7.2m$ downstream of the object position, behind a He-filled flight tube to prevent excessive absorption and scattering by air.

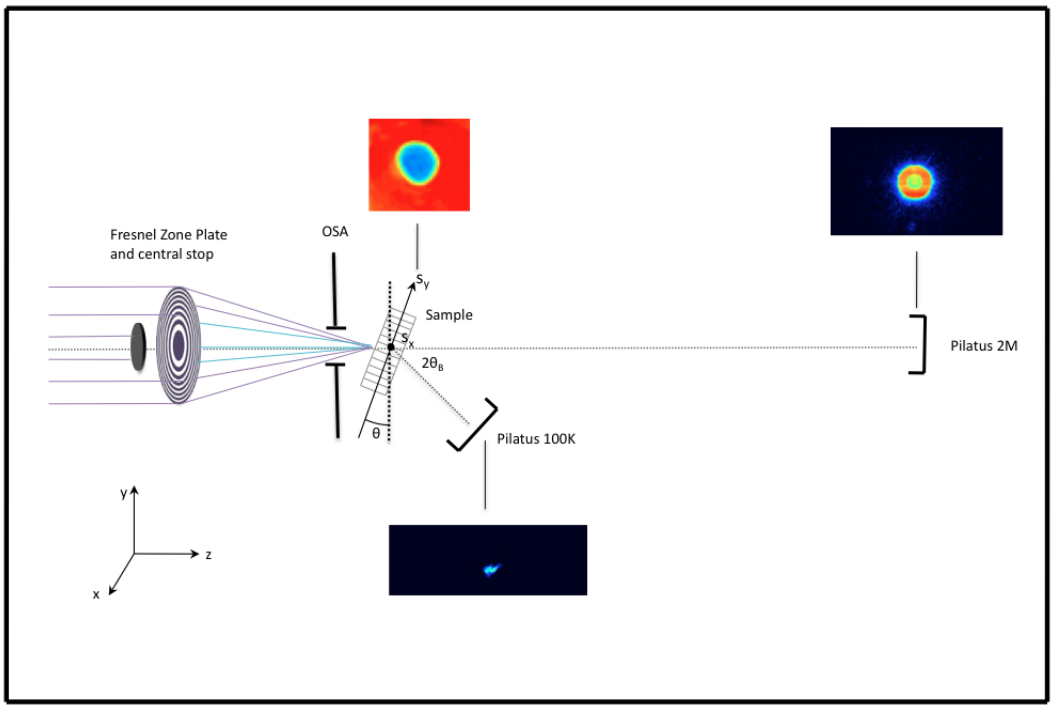

Figure 4.1: Setup schematic. The sample is represented showing the 111 diffraction planes and it can clearly be seen that the two detectors collect the transmitted beam (Pilatus 2M) and the reflected beam at Bragg angle (Pilatus 100k).

[1]When the X-Ray beam hits the FZP, the radiation is affected by both phase shift and attenuation. This is due to the complex refractive index of gold $n = 1 - \delta + i\beta$ [7], where δ is related to the scattering properties of the medium ($1 - \delta$ refers to to the radiation velocity in the substance) and β is the absorption coefficient. In our case, at $8.7KeV$ we have $\delta = 4x10^{-5}$ and $\beta = 3.75x10^{-6}$. By considering the FZP's 1μm thickness it is possible to get a phase shift of $\Delta\phi = \frac{2\pi\delta t}{\lambda} = 1.76rad$ and an attenuation of $a = 1 - e^{-\frac{2\pi\beta t}{\lambda}} = 15\%$. The probe, which is the focused beam obtained after the FZP-OSA cascade, has in fact its own phase and amplitude which result from the propagation of the beam passing through the system. This is taken into account during the reconstruction procedure and what we get in the end is only the object's phase and amplitude.

The PILATUS 100k used a single module of 195×487 pixels and was inclined at 35°with respect of the propagation axis (z), at a distance of 1.03m from the sample. We have looked at 250nm gold nanocrystals, grown on a 100nm thick SiN membrane. The SEM analysis confirmed that crystals were approximately 250nm in diameter and spaced approximately 1µm apart.Ptychographic acquisitions were then performed in order to retrieve both amplitude and, more important, phase of the sample.

The expected beam size for this experiment is equal to the FZP outermost zone width (100nm), but a more precise estimation can be done by analyzing the reconstructed probe profile (Fig.4.3).

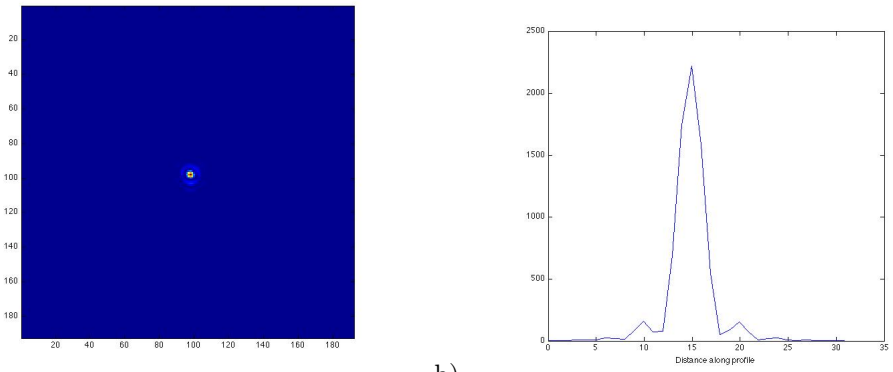

a) b)

Figure 4.2: Reconstructed probe intensity a) and linear profile b).

The beam size can be retrieved by measuring the FHWM in the probe linear profile and by multiplying it by the pixel size at the sample plane which for this configuration is around 31nm.

$$pix_{sample} = \frac{\lambda z}{npix_{det}} \tag{4.1}$$

where z is the sample-detector distance, in this case 7.2m in the forward direction and n is the recorded data array size, 192 for us. The result is a beam size of around 110nm which is consistent with what expected.

At the beginning of the experiment we made sure that theX-Ray beam was hitting the -111 plane at the Bragg angle, which for this condition is 17.65°. By already knowing the nature of our crystals we had the idea that the Bragg condition could have been easily met by keeping the sample more or less perpendicular to the beam. In order to do that, we scanned with the piezo stage along the sample (xy plane) to find a crystal. The presence of the crystal was observed in reflection by seeing a bright spot on the PILATUS 100k as seen on Fig4.3. After finding the crystal we did a rocking scan by moving the ϑ angle to really find the Bragg reflection which is related to the highest intensity sampled on the PILATUS 100k (Fig 4.3 a). Once observed the correct Bragg angle we defined a set of angles around it in order to perform reconstructions on and off the Bragg. The whole set of positions is observed in a rocking curve where the integrated intensity is plotted at each angle.

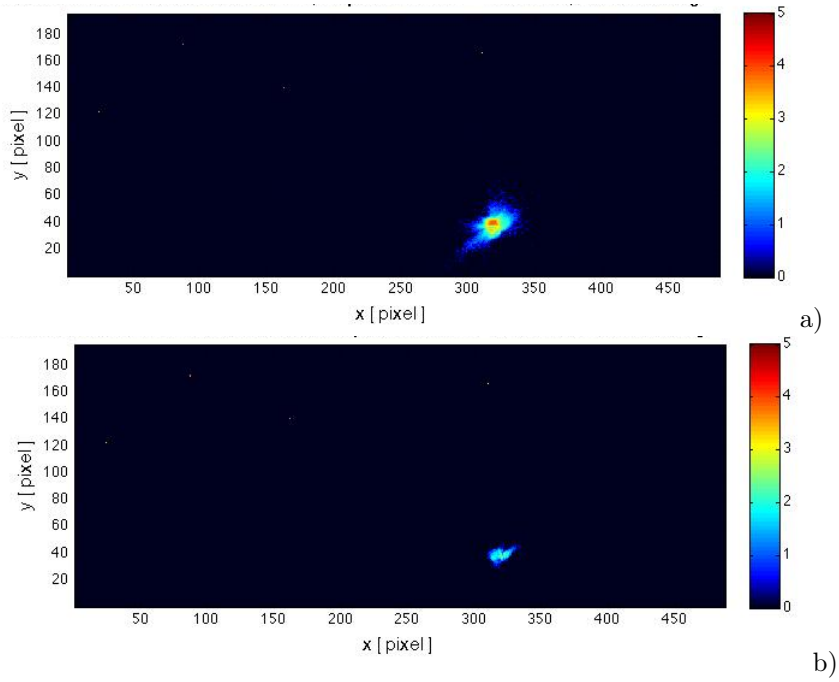

Figure 4.3: Recorded intensity on PILATUS 100k. In a) the Bragg angle is detected, while in b) the weaker intensity confirms that we are off the Bragg.

The rocking curve for a set of nine scans around the Bragg angle can be observed in Fig.4.4.

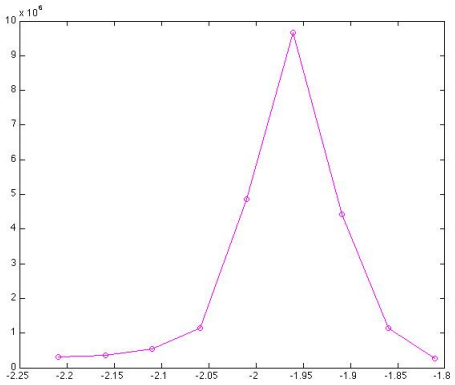

Figure 4.4: Rocking curve for a set of scans.

Once defined the rocking curve, we performed a series of ptychographic acquisitions by circular-scanning

the sample.

4.1.2 Data analysis

For each scan I performed a ptychographic reconstruction by using a code based on the difference map method. I have been able to obtain the reconstructed sample in both amplitude and phase as well as the reconstructed probe for most scans.

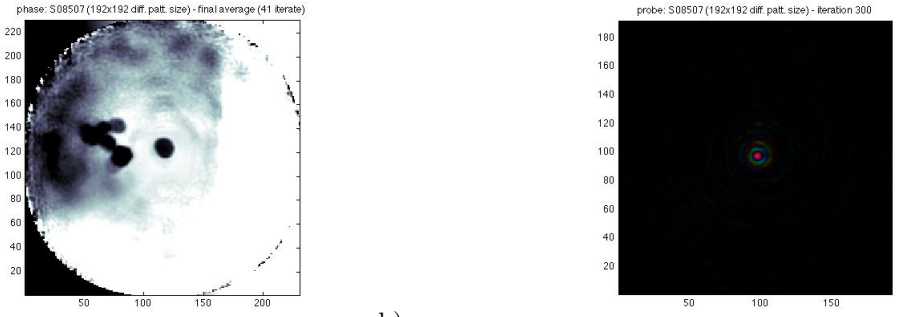

a) b)

Figure 4.5: Reconstructed sample phase a) and probe b)

Since the aim of our experiment was to observe a phase shift when rocking the ϑ angle around the Bragg condition I concentrated on each set of scans separately. I have processed all reconstructions in each set in order to remove the inevitable phase ramps and to make a comparison between scans possible.

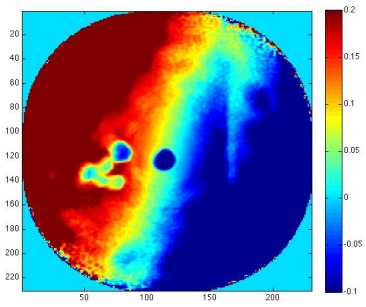

Figure 4.6: Phase ramp on the reconstructed sample.

The phase ramp removal method which I used was based on the search of gradients in the reconstructions. In order to use it, it was also necessary to draw masks around the crystal in the region of interest[2]. The

[2]This method can be easily described in the 1D case, if considering that a phase ramp can be pictured as a line of a certain

above figure also shows that during each reconstruction the field of view also included other structures as well as the edge of the sample support. This of course contributed to the formation of the phase ramp. For this reason and to better analyze the reconstructions I decided to define a region of interest around the crystal and to only concentrate on that portion of the reconstructed phase. One other issue I have encountered was relative to the drift of the sample. In fact since we performed very long acquisitions during our experiment (usually 456 points for each ptychographic scan) a drift of the sample was inevitable. In order to compare all phase profile I also needed to align all reconstructions after getting rid of the phase ramp.

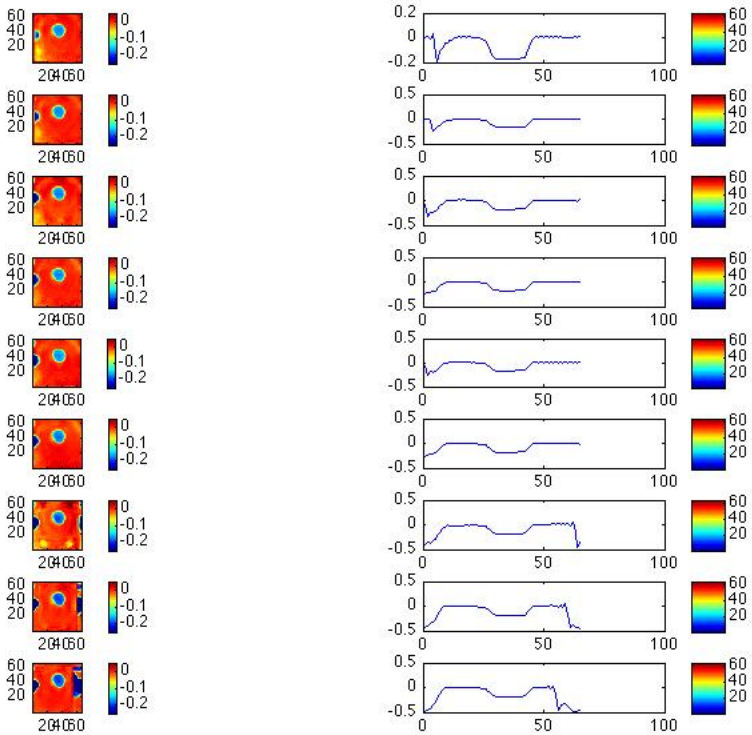

Figure 4.7: Reconstructions alignment and linear phase profile.

The profiles on the right of Fig 4.7 were obtained by selecting one line in the reconstructed phase and by plotting the variable phase as a function of the pixel position. If compared, the phase profiles show a phase shift inside the sample (Fig.4.8).

inclination. In order to get rid of that it is necessary to calculate the gradient of the phase in our reconstructed data, along x for instance, and to get its average in the region defined by the mask, an x interval in the 1D case. Once this has been done, this mean value is used to correct the phase ramp by changing its sign and by multiplying it by the initial x values.

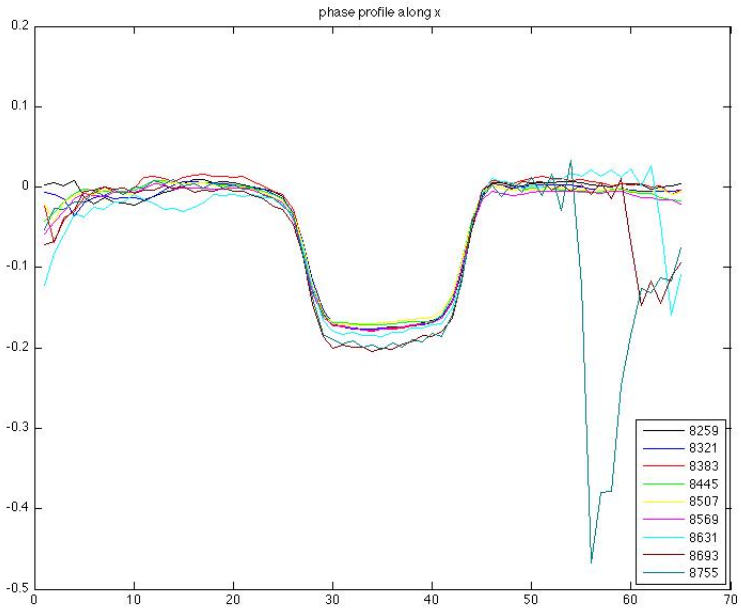

Figure 4.8: Phase profiles in a set of nine scans taken at different angle around the Bragg. The phase shift given by the X-Ray beam passing through the gold nanocrystal is 0.2 rad, as expected by the theory. The maximum phase shift inside the crystal, which we obtained by rocking the sample around the Bragg condition, is around 0.03 rad.

It appears clear that in order to establish if the observed phase shift inside the crystal could really be quantified in 0.03 rad, further analysis were needed. In particular I wanted to make sure that the noise outside the crystal was negligible if compared with the phase shift inside the crystal itself. For this reason I wrote a Matlab routine to draw boxes outside and inside the crystal. I then used the phase values in each box to estimate the mean value and the standard deviation. In this way I was able to calculate the error which affected the reconstructions and to define error-bars which helped to establish if the phase shift inside the crystal was bigger than the noise or not.

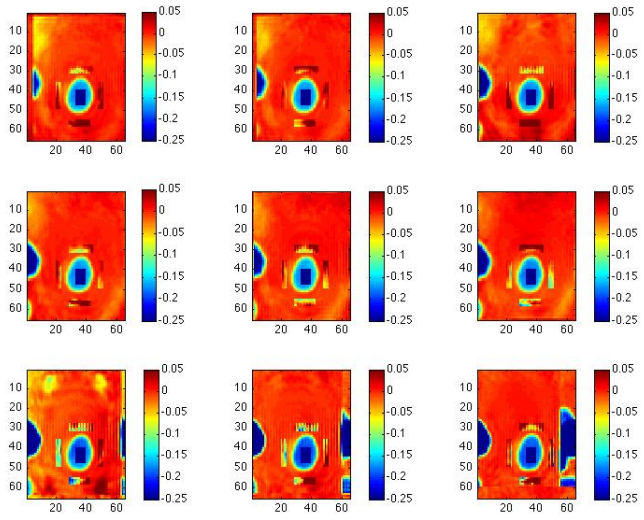

Figure 4.9: Boxes used to calculate the mean value and the standard deviation of the phase inside and outside the crystal.

In the end I obtained a graphic of phase versus angles showing nine points and error-bars. The phase value for each scan (identified by the correspondent angle) was calculated as

$$phase_{av} = phase_{av,c} - \frac{phase_{av,1} + phase_{av,2} + phase_{av,3} + phase_{av,4}}{4} \tag{4.2}$$

where $\text{phase}_{\text{av,c}}$is the average phase calculated in the box inside the crystal and $\text{phase}_{\text{av,i}}$are the phases calculated in the four boxes outside the crystal. The error-bars were calculated for each scan by combining the standard deviation of the phase in each box following the formula

$$\varepsilon_{tot} = \sqrt{\varepsilon_c^2 + \frac{1}{16}\varepsilon_1^2 + \frac{1}{16}\varepsilon_2^2 + \frac{1}{16}\varepsilon_3^2 + \frac{1}{16}\varepsilon_4^2} \tag{4.3}$$

where $\varepsilon_{\text{i}}$are the squared standard deviation inside and outside the crystal.

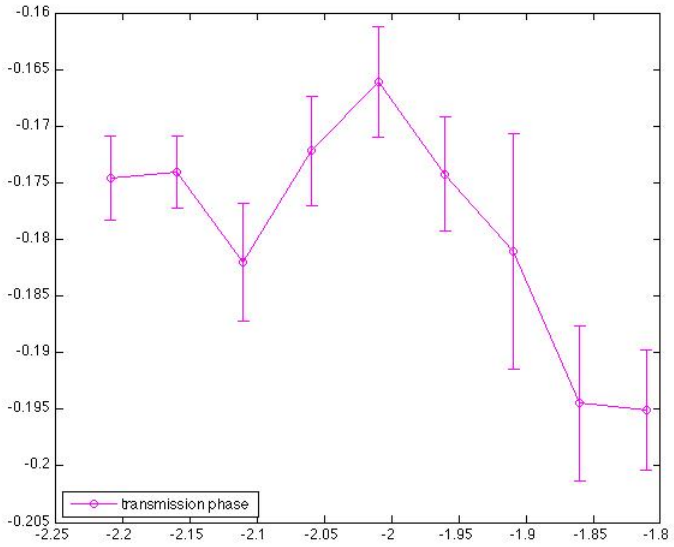

Figure 4.10: Error-bar plot showing the phase shift. The error-bars have been plotted with amplitude of $\pm\varepsilon_{\mathrm{tot}}$. The plot is centered around the Bragg angle position and it is possible to see that the maximum phase shift between the on and off Bragg conditions is around 0.03 rad, as previously showed in Fig. 4.8.

In order to make sure that this effect was also present in other sets of acquisitions, I also performed the data analysis, following all steps described above, for all our data. Besides the fact that the results I have been showing so far are relative to the biggest set we collected (nine scans well placed around the Bragg angle), a trend in the phase shift appears evident (Fig.4.11). It is worth noticing that all scans refer to the same crystal and in the figure are all centered around the Bragg. I also decided to include a set containing a bad reconstruction (the one drawn in red clearly shows a point which represents a bad reconstruction) to show that even in that case the trend is still visible if considering the well reconstructed scans of that series.

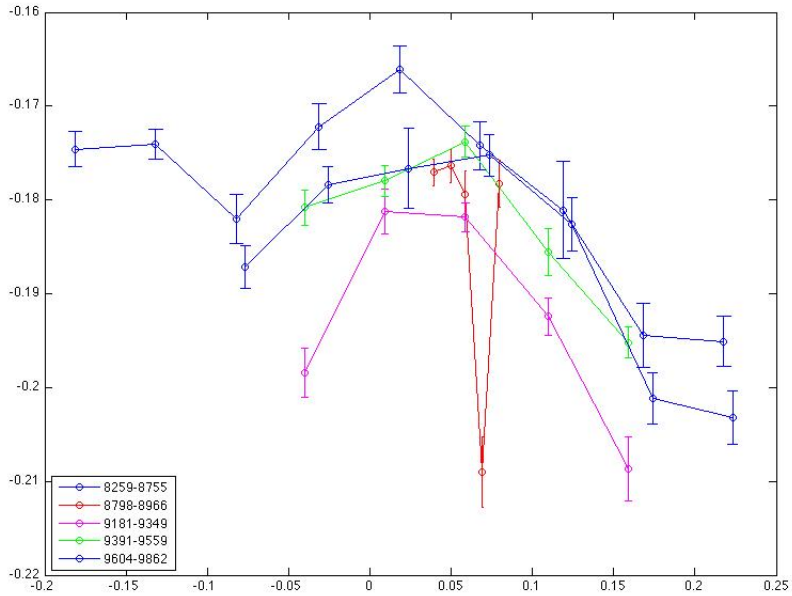

Figure 4.11: Phase shift trend in various sets of scans. In this figure all curves have been shifted so that the Bragg position is set to zero.

4.1.3 Theoretical background

We started this experiment with the aim of investigating the dynamical domain, which exists when diffraction takes place inside a thick crystal. In this case the dynamical theory describes how the scattered waves, emerging from various crystallographic planes, interact to define a total wave field inside the crystals. What results from this regime is well known from the theory but has never been empirically demonstrated and this explains why we are interested in this subject [49].

In this paragraph I will not give an explanation related to the dynamical theory because, due to the small thickness of our sample, it has been easier to describe the phase shift with the kinematical theory. At present we are collaborating with experts in the field who might be able to relate our results to the dynamical effect, but even in the case this will not be possible, we are satisfied by our results because we understand that our experimental method is correct and we are very close to really investigate the dynamical regime. To this purpose we are already applying for beamtimes to repeat this experiment with more suitable samples.

The kinematical theory treats the scattering from each volume element in the sample as being independent of that of other volume elements [49]. In this case I will consider a simple lattice in the Laue geometry.

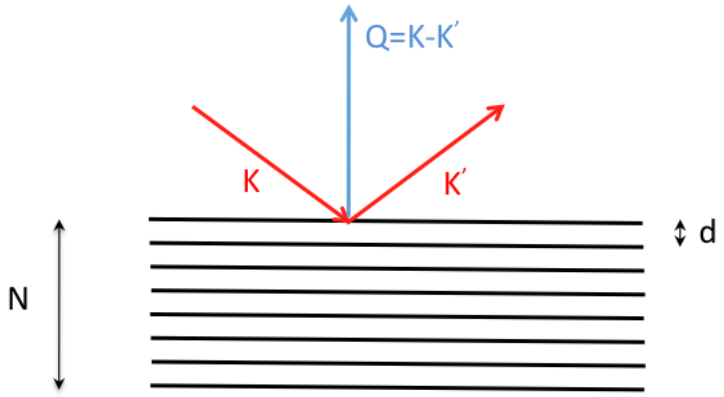

Figure 4.12: Lattice in the Laue geometry. An incident wave and the corresponding scattered one are showed for one plane, as well as the resulting scattering vector Q. If we extend this treatment to all planes, we get a superposition of Q vectors.

The first thing that I did was to calculate the rocking curve, in order to understand if what we retrieved from the experimental data was consistent with the theory. In this situation a very intuitive treatment is to calculate the sum over the N planes (where N is related to the thickness of the crystals) of the reflected waves. The distance between two contiguous planes is related to the lattice constant a by the formula

$$d = \frac{a}{\sqrt{h^2 + k^2 + l^2}} \tag{4.4}$$

where h, k and l are the Miller indices for the set of planes being considered. In our case we were considering the -111 set of planes and I got $d = 2.35\dot{A}$. By only concentrating on the phase factors, it is possible to say that the resulting phase is given by the geometrical series

$$R_N(\mathbf{Q}) = \mathbf{A} \sum_{\mathbf{j=0}}^{\mathbf{N-1}} \mathbf{e^{iQ \cdot d_j}} = A \frac{1 - e^{iQNd}}{1 - e^{iQd}} \tag{4.5}$$

being A the amplitude which we adjusted in order to fit our data. The experimental rocking curve is calculated staring by the intensities collected on the PILATUS 100k, so in order to compare the two curves I calculated

$$I_R(\mathbf{Q}) = |R(\mathbf{Q})|^2 \tag{4.6}$$

which is plotted in the following figure.

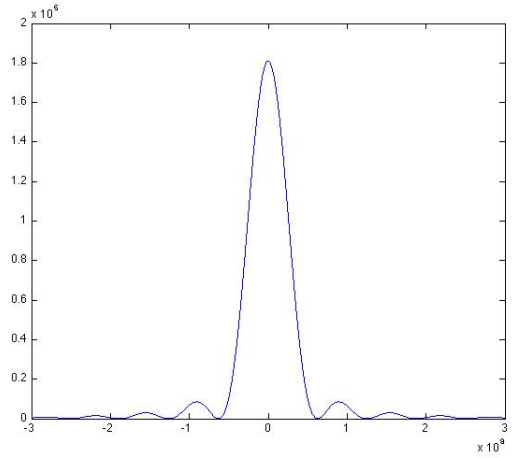

Figure 4.13: Theoretical rocking curve calculated for a crystal 100nm thick with $A = 1$.

The transmitted wave in the forward direction can be easily calculated from the reflected beam by considering that the conservation of energy requires the transmitted amplitude to be reduced when a beam is diffracted away, but it's a complex amplitude since everything is coherent. It is then possible to write

$$T(\mathbf{Q}) = 1 - \alpha R(\mathbf{Q}). \tag{4.7}$$

At this point the transmitted wave is a complex function whose phase is plotted in Fig. 4.14.

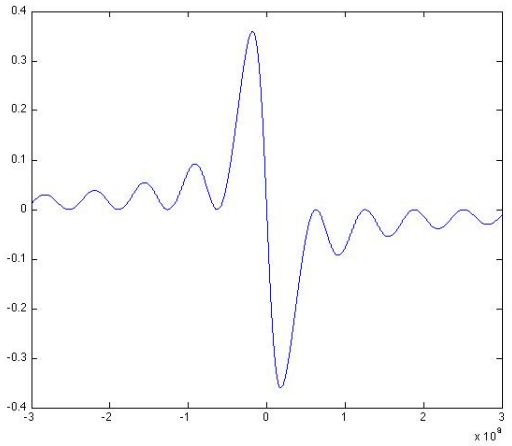

Figure 4.14: Theoretical transmitted phase. $\alpha = 0.001$.

It was now possible to compare our experimental results with these theoretical results.

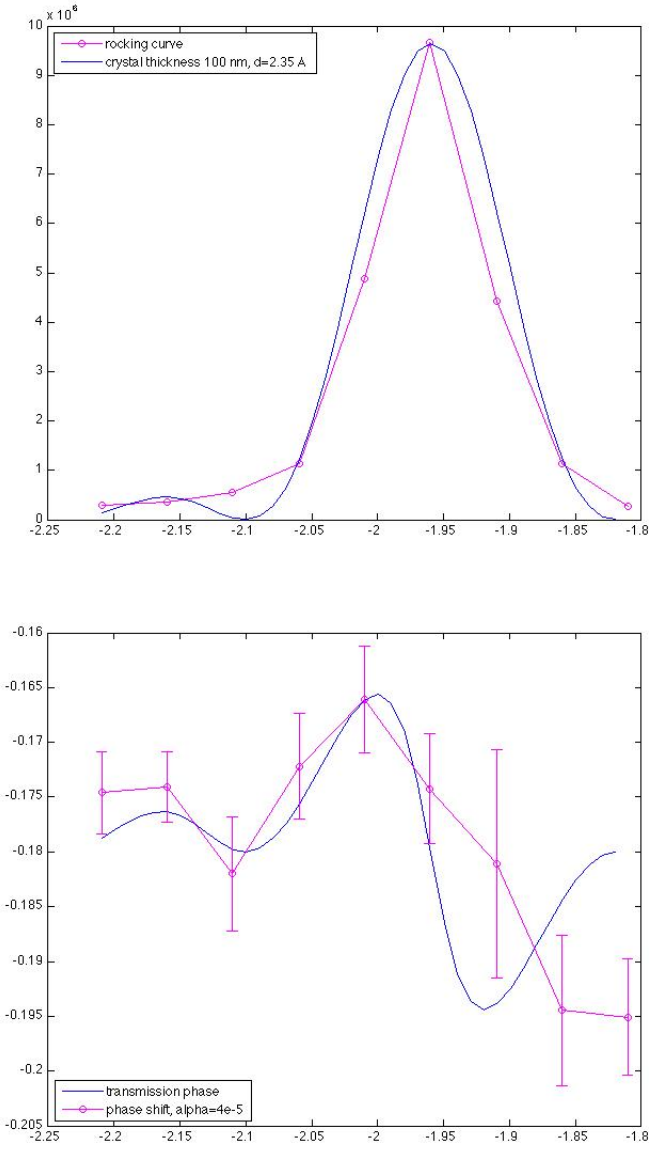

Figure 4.15: At the top is the rocking curve fitting which we obtained for a 100nm thick crystal. At the bottom is the phase shift fitting where $\alpha = 4 \cdot 10^{-5}$. The Bragg angle is t the middle of the rocking curve at -1.96 degrees. This fitting has been done by manually adjusting the coefficients.

This result shows a measurable phase shift even in the kinematical limit. It is possible to see that the

phase of the structure factor of a finite crystal varies across the rocking curve and this causes an angle-dependent phase shift in the transmitted beam also. It is worth pointing out that the lack of symmetry in the retrieved phase shift profile is due to a series of less accurate reconstructions for those positions at the end of the rocking curve (also the error-bars are indeed much bigger for these scans). This was mainly due to the drifting of the sample because, as previously stated, one mistake during our experiment was to run too long scans.

4.2 The siemens star

During a recent experiment conducted at the APS 34ID-C beamline we managed to observe a peculiar effect which provoked our interest. The aim of that beamtime was mainly to develop ptychography in the beamline, which was more specialized in CDI. In this experiment the beam was focused with the use of KB mirrors and we had a downstream 3D piezo stage to scan the sample. The diffraction patterns were recorded in transmission with the aid of a 20 microns CCD camera.

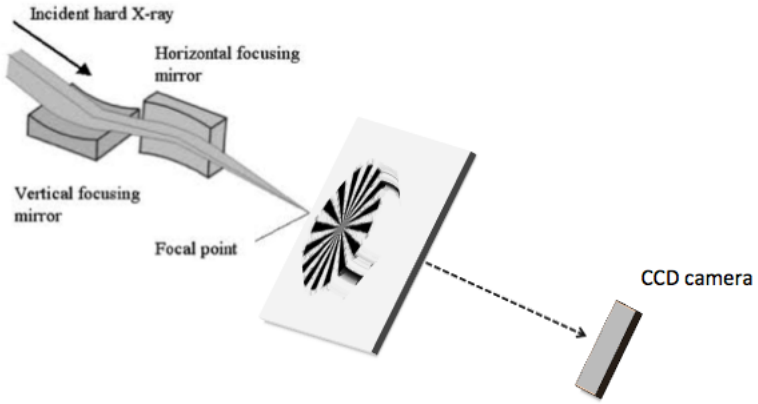

Figure 4.16: Experimental setup used to reconstruct a 1.5 um thick tungsten siemens star deposited on a silicon nitride support film (100 nm). The distance between the KB mirrors and the sample was around 80mm.

The experiment was performed in such a way that we collected a various set of diffraction patterns at different distances, by moving the CCD camera, and for different beam sizes which were obtained by adjusting the JJ slits gap. The JJ slits are located 27.5 m in front of the coherence-defining entrance slits and are used to select the coherent part of the incident X-ray beam. The aim of this experiment was to retrieve the probe in all conditions and to test the ability of the ptychography algorithm to reconstruct the object close to the near field condition and for different beam's coherences. The JJ slits apertures were three: 10umX10um (small beam), 30umX50um (big beam) and 25umX25um (intermediate condition). As explained in Chapter

2, the different slits aperture leads to a change in the beam's coherence: the closer the slits, the higher the coherence. The CCD camera distances were 0.55, 1 and 2.129 meters. Another reason for this kind of measurement was the idea of binning the different datasets so to compare the results with the unbinned ones at different distances: for example bin by a factor of 2 the 1m dataset and compare it with the unbinned one at 0.55m.

When reconstructing the test samples we obtained both phase and amplitude of a 36 spokes simemens star whose position in the original layout is showed below.

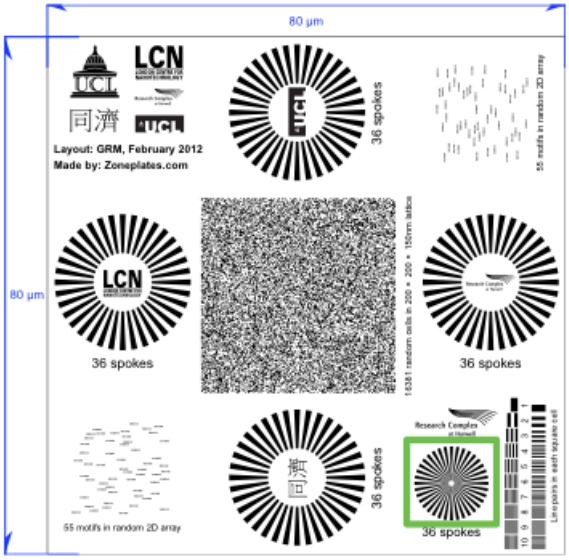

Figure 4.17: Test sample layout. The green square shows the portion of test sample reconstructed in our experiment.

The interesting effect that we immediately noticed was that by changing the detector distance in the reconstruction algorithm for the same dataset, we obtained a siemens star with a different number of spokes but same in size.

We concentrated our interest on a dataset recorded at 0.55m downstream from the sample, with a JJ slits aperture of 30umX50um (horizontal X vertical direction). If in the correct reconstruction we were able to get the real siemens star, we saw that there was a reduction in the number of spokes when increasing the distance and the inverse trend when going to the opposite direction. It was also interesting to notice that the number of spokes was related to the sample-CCD camera distance in such a way that if for the real sample position we counted 36 spokes, we got 72 at half the distance (25.5 cm) and 18 at twice the distance (1.1m). As showed in Fig. 4.18 the number of spokes changes continuously in the intermediate positions.

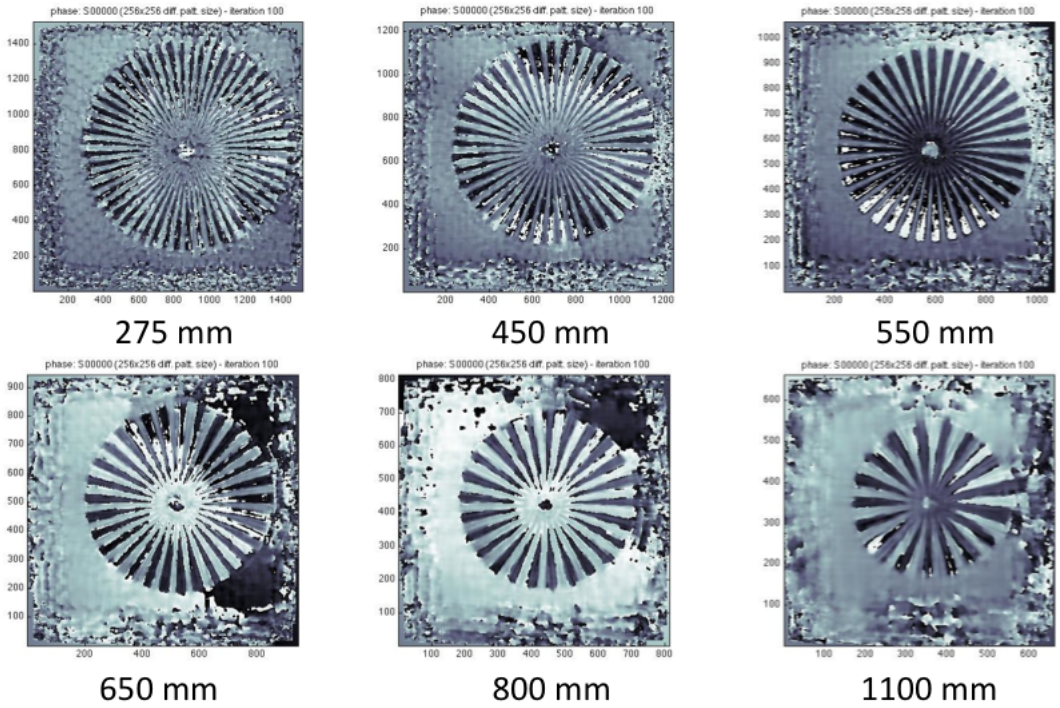

Figure 4.18: Reconstructions of a 36 spokes siemens star when simulating a set of different distances. The 'real' reconstruction is the one performed at 0.55m.

We tried to explain this effect by referring to the Talbot self-imaging effect which is a near field effect, consequence of Fresnel diffraction. The Talbot effect is depicted by the case of a wave illuminating a periodic diffraction grating. In this case the image of the grating is repeated at regular distances away from the grating plane. The regular distance is called the Talbot length, and the repeated images are called self images or Talbot images. We believed that this situations was similar to ours due to the symmetrical geometry of the siemens star which can be considered as a sort of varying step grating (for example considering the varying spoke width). In order to get a theoretical support for our experiment and to compare it with the Talbot effect, we propagated the 36 spokes siemens star at different distances, multiple of the Talbot distance $D_T = 2a^2/\lambda$ (where a is the grating step). Unfortunately we did not find any similarity between the simulated Talbot effect and our reconstructions. This experiment is still in the process of being analyzed and the following results will soon be submitted for publication.

Chapter 5

Future work

During this first part of my Phd I have been involved in many subjects and so for this reason there are many fields which I intend to investigate before completing my studies. Before going into a brief overview of what I practically intend to do in the next part of my Phd, I want to report a new result about the experiment on gold nanocrystals.

I have already described how gold nanocrystals are not well suited for investigating the dynamical diffraction regime, relating this to their small thickness. Because this is very much a work in progress, I want to include in this chapter a new result gently provided by Prof. Ivan Vartaniants, a recognized expert in the field, which actually demonstrates that the above statement is not true. He was able to fit my experimental results by using the dynamical theory as showed in Fig. 5.1.

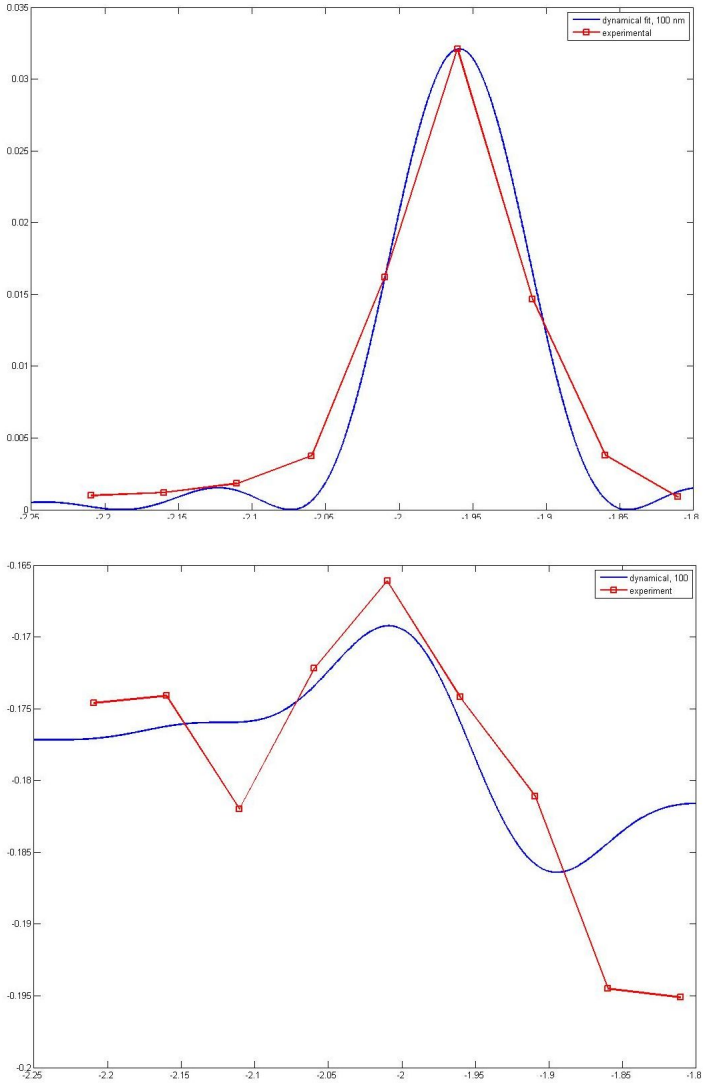

Figure 5.1: Rocking curve (up) and phase shift (down) fittings for a 100nm thick gold nanocrystal. Results obtained with the use of dynamical diffraction theory equations. Calculations gently provided by Prof. Ivan Vartaniants.

This result is again affected by the lack of symmetry and all the problems already discussed in the previous chapter, yet it clearly demonstrates a phase shift in the dynamical regime. At this moment my first urgency is then to become extremely familiar with the dynamical theory of diffraction. I already have quite a list of books and articles to study so I would say that is my most immediate future work to do.

Until a couple of weeks ago, I thought that gold nanocrystals were not suitable to give evidence to

dynamical diffraction effects and for this reason I had already submitted a series of new proposals with the aim of repeating that experiment with a new set of samples, consisting of silicon pillars obtained by etching 110 and 100 monocrystalline wafers. Besides being encouraged by the results obtained with gold nanocrystals, I still think that these new samples are going to make it easier to see dynamical effects. The key feature of the new samples is their geometry. Because we want to observe the Bragg condition relative to the 111 plane of Si, we prepared our pillars in such a way that a beam almost perpendicular to the facet will easily be able to reach the requested angle. For the 110 samples both transmitted and 111 Bragg reflected beams lie in the same plane as the wafer, while for the 100 wafer, the 111 diffracted beam will be inclined above the plane.

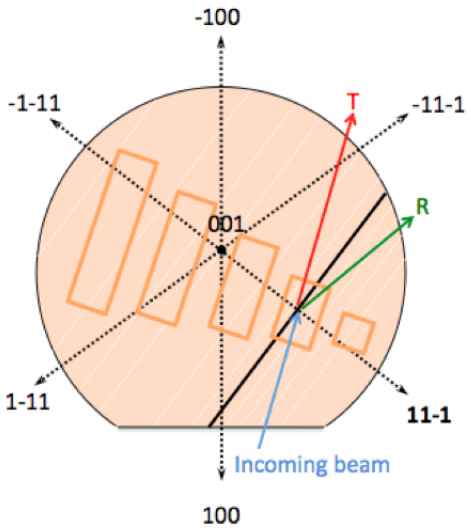

Figure 5.2: Schematic representation of how we plan to cut our pillars out of a 100 silicon wafer. After identifying the 111 crystallographic direction (11-1 in the figure) we consider its perpendicular set of planes (black bold line and white lines). The idea of the experiment is to perform a series of acquisitions (ptychographic scans) around the Bragg angle. In order to simplify the setup we plan to cut our pillars (orange rectangles-top view) in such a way that the incoming beam at the Bragg angle (blue arrow) is already perpendicular to the pillars facets.

The single sample consists of a silicon support with a set of equally spaced Si pillars at the top (all obtained as a single piece from etching the wafer), all with different thicknesses (2 to 20 microns) but same width (2microns) chosen to match the piezo scan range (see Fig.5.3). In this way we should also be able to see how the phase shift changes in relation with the sample's thickness.

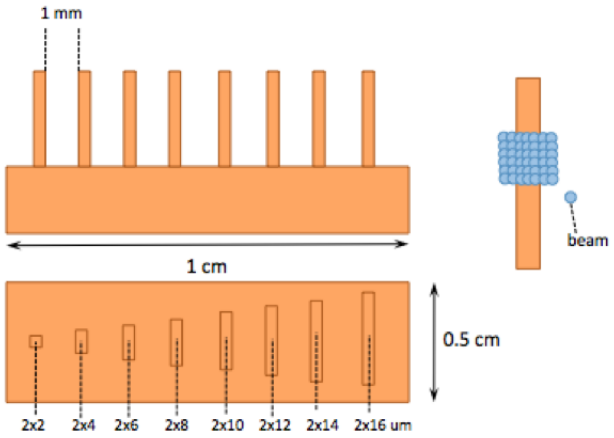

Figure 5.3: Lateral (up) and top (down) views of our sample. We are producing a set of Si pillars with same height (100um) and lateral profile (2um) but different thickness (from 2 to 16um). The pillars are obtained by etching the silicon wafer so that their support is part of the original wafer itself. On the side is an example of how to perform a ptychographic acquisition.

The experiment on gold nanocrystals has been at the center of my work for a long time. The final part of this will be to publish a paper on the results provided in the previous chapter. I also believe that there is a further analysis which can be conducted by considering the data collected in the reflection geometry.

During my first year I managed to use ptychography to reconstruct the phase and amplitude of a gold nanocrystal in the reflection geometry and it was so possible to compare this result with the one obtained in transmission.

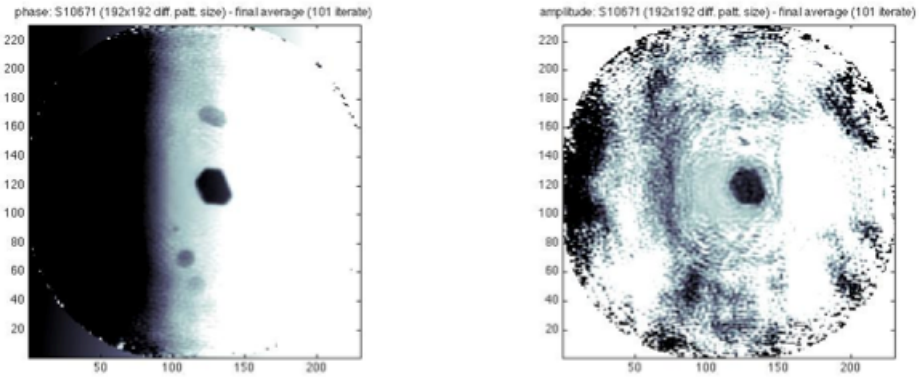

Figure 5.4: Reconstruction of both phase (l) and amplitude (r) of a gold nanocrystal in the transmission geometry. The algorithm used was based on the Difference Map approach.

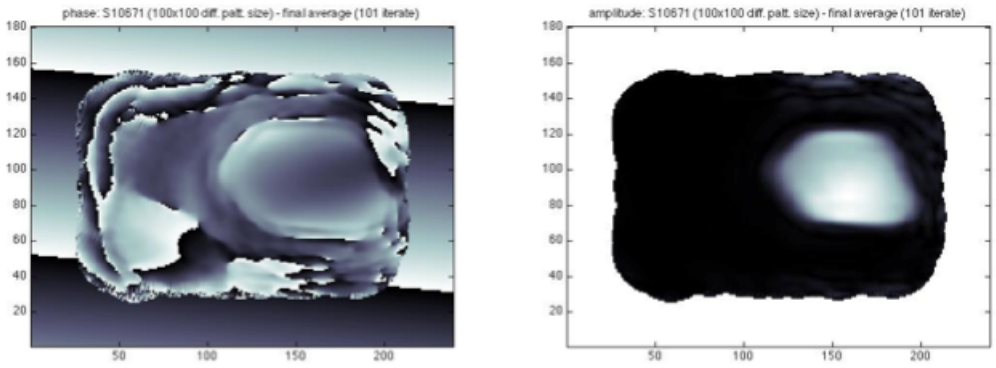

Figure 5.5: Reconstructed phase (l) and amplitude (r) of a gold nanocrystal in the reflection geometry.

This result was quite unique because I only managed to obtain a good reconstruction for few datasets in proximity of the Bragg condition. This can be explained by the fact that the diffracted intensities in the reflection geometry (collected by the inclined PILATUS 100k) are strong at the Bragg angle and very week off the Bragg condition. It is also worth noticing that in order to reconstruct this crystal, we modified the probe used in the transmission geometry by rotating it to the PILATUS 100K plane. This approach is well described in Richard Bean's Phd Thesis [6]. The reason of my interest in these datasets collected in the reflection geometry is that it is possible to combine them with the ones collected in transmission to get a 3D reconstruction of the gold nanocrystals. This is something I have already discussed with Dr. Ana Diaz and Dr. Manuel Guizar Sicairos, beamline scientists at the cSAXS beamline, and I believe that it can be done. There is not a consolidated method for obtaining this kind of 3D reconstructions, so I will need to invent one starting from the suggestions provided from both literature and collaborations. The final goal of this further data analysis will be to publish a second paper on this experiment, being the first one based on the phase shift effect.

The last thing that I would like to do during my Phd is quite an ambitious project on Ptychography. So far I have always used working algorithms developed by other teams or researchers and the natural next step in my work is to write my own code. In order to do that I have managed to become more familiar with the Matlab programming tool, which I did not know at the beginning of my Phd. Of course my purpose is to give my own contribution to the field, rather than only re-writing some already existing codes. I have already thought about several ways to improve the algorithm. The first idea is to vary the overlap region when using the probe to scan the object. This idea came to my mind because, as stated in [6] but also as it is widely discussed in the literature, it has been seen that usually breaking the symmetry in the acquisition procedure can improve the reconstruction. This can be done in several ways and the idea of changing the overlap region is one of those. I have already discussed this idea with Dr. Manuel Guizar Sicairos during a recent visit to SLS and he told me that he has already tried this with no improvement in the reconstruction.

I did not have time to test it myself, but I eventually will. Another way to improve the algorithm could be to use both ePIE and DM in the same code and skipping from one to the other during the iterations. This may help to get a faster convergency. In addition to that I could implement in my algorithm the probe position correction developed by one of my group members, Dr. Fucai Zhang [50]. The last possible way of improving my code will be to implement new algorithms like a 2D adaption of the multi-slice approach [51] and other extremely recent methods [52, 53].

Bibliography

[1] Takeo Kamino Joachim Mayer, Lucille A. Giannuzzi and Joseph Michael. Tem sample preparation and fib-induced damage. *MRS Bulletin*, 32:400–407, May 2007.

[2] Susan Swapp. Scanning electron microscopy (sem). *University of Wyoming, Geochemical Instrumentation and Analysis department.*

[3] H. Rohrer G. Binnig. Scanning tunneling microscopy. *IBM Journal of Research and Development*, 30:4, 1986.

[4] Gerber Ch. Binning G., Quate C. F. Atomic force microscope. *Physical Review Letters*, 56:930:936, 1986.

[5] C. Jacobsen J. Kirz and M. Howells. Soft x-ray microscopes and their bio- logical applications. *Quarterly Reviews of Biophysics*, 28(1):33–130, 1995.

[6] Richard Bean. *Domain Structure Imaging with Bragg Geometry X-ray Ptychography.* PhD thesis, London Centre for Nanotechnology, University College London, 2012.

[7] McMorrow D. Nielsen J.A. *Elements of Modern X-ray Physics.* Wiley, 2011.

[8] Baez A. Kirkpatrick P. Formation of optical images by x-rays. *Journal of the Optical Society of America*, Vol 38, Num 9:766–774, 1948.

[9] Snigireva et. Refractive x-ray lenses. *Journal of Applied Physics*, 38:218–222, 2005.

[10] W Chao. Soft x-ray microscopy at a spatial resolution better than 15 nm. *Nature*, 435:1210–1213, 2005.

[11] Schmahl G. Niemann B., Rudolph D. X-ray microscopy with synchrotron radiation. *Applied Optics*, 15:1883–1884, 1976.

[12] M. Lerotic. *Finding the patterns in complex specimens by improving the acquisition and analysis of x-ray spectromicroscopy data.* PhD thesis, State University of New York at Stony Brook, 2005.

[13] Kirz J. Howells M. R. Chang P. Coane P.J. Feder R. Houzego P. J. Kern D. P. Sayre D. Rarback H., Kenney J. M. Recent results from the stony brook scanning microscope. *X-Ray Microscopy*, 43:203–215, 1984.

[14] Jacobsen C. Hornberger B., Feser M. Quantitative amplitude and phase contrast imaging in a scanning transmission x-ray microscope. *Ultramicroscopy*, 107:644–655, 2006.

[15] M. G. L. Gustafsson. Surpassing the lateral resolution limit by a factor of two using structured illumination microscopy. *Journal of Microscopy*, 198:82–87, 2000.

[16] Shao L. Carlton P. M. Wang C. J. R. Golubovskaya I. N. Cande W. Z. Agard D. A. Sedat D. A. Gustafsson, M. G. L. Three-dimensional resolution doubling in wide-field fluorescence microscopy by structured illumination. *Biophysical Journal*, 94:4957–4970, 2008.

[17] Juskaitis R. Wilson T. Neil, M. A. A. Method of obtaining optical sectioning by using structured light in a conventional microscope. *Optics Letters*, 22(24):1905–1907, 1997.

[18] Juskaitis R. Wilson T. Neil, M. A. A. Real time 3d fluorescence microscopy by two beam interference illumination. *Optics Communications*, 153:1–4, 1998.

[19] Squire A. Juskaitis R. Bastiaens P. I. H. Wilson T. Neil, M. A. A. Wide-field optically sectioning fluorescence microscopy with laser illumination. *Journal of Microscopy*, 197:1–4, 2000.

[20] Herriott H. D. Gallagher J. E. Rosenfeld D. P. White A. D. Brangaccio D.J. Bruning, J. H. Digital wavefront measuring interferometer for testing optical surfaces and lenses. *Applied Optics*, 13(11):2693–2703, 1974.

[21] Gao M Zhang R Nagahara LA. Zuo JM, Vartanyants I. Atomic resolution imaging of a carbon nanotube from diffraction intensities. *Science*, 300(5624):1419–21, 2003.

[22] Onken J.D. Pfeifer M.A. Williams G.J. Pfeiffer F. Metzger H. Zhong Z. Bauer G. Vartanyants I.A., Robinson I.K. Coherent x-ray diffraction from quantum dots. *Physical Review B: Condensed Matter and Materials Physics*, 71:245302, 2005.

[23] Bates R.H.T. Fourier phase problems are uniquely sol- uble in more than one dimension.i: underlying theory. *Optik*, 61:247–262, 1982.

[24] Theory of signals class notes. Technical report, Politecnico di Milano.

[25] Chapman H. N. Miao J., Sayre D. Phase retrieval from the magnitude of the fourier transforms of nonperiodic objects. *J. Opt. Soc. Am.*, 15(6):1662–1669, 1998.

[26] Newsam G. Barakat R. Necessary conditions for a unique solution to two-dimensional phase recovery. *journal of Math. Phys.*, 25:3190–3193, 1984.

[27] J. R. Fienup. Phase retrieval algorithms: a comparison. *Applied Optics*, 21:2758–2769, 1982.

[28] Wackerman C. C. Fienup, J. R. Phase-retrieval stagnation problems and solutions. *J. Opt. Soc. Am.*, 3:1897–1907, 1986.

[29] M. Howells. Coherent x-rays and their applications, lecture 1. In *ESRF Experiments Division*.

[30] Hoppe W. Hegerl R. Ber. bunsenges. *Ptys. Chem*, 74:1148, 1970.

[31] Nellist P.D. Rodenburg J.M. Electron ptychography i: experimental demonstration beyond the conventional resolution limits. *Acta Crystallographica*, 54:49–60, 1998.

[32] Plamann T. Rodenburg J.M. Electron ptychography ii: theory of three-dimensional scattering effects. *Acta Crystallographica*, 54:61–73, 1998.

[33] Cullis A.G. Dobson B.R. Pfeiffer F. Bunk O. David C. Jefimovs K. Johnson I Rodenburg J.M., Hurst A.C. Hard-x-ray lensless imaging of extended objects. *Physical Review Letters*, 98, 2007.

[34] Maiden A.M. Rodenburg J.M. An improved ptychographical phase retrieval algorithm for diffractive imaging. *Ultramicroscopy*, 109:1256–1262, 2009.

[35] Rodenburg J.M. Ptychography and related diffractive imaging methods. *Advances in Imaging and Electron Physics*, 150:87–184, 2008.

[36] Schopp A. et all. Non-destructive and quantitative imaging of a nano-structured mi- crochip by ptychographic hard x-ray scanning microscopy. *Journal of Microscopy*, 241:9–12, 2011.

[37] Dierolf M. et all. Ptychographic coherent diffractive imaging of weakly scattering specimens. *New Journal of Physics*, 12:035017, 2010.

[38] Giewekemeyer K et all. Quantitative biological imaging by ptychographic x-ray diffraction microscopy. *Proceedings of the National Academy of Sciences*, 107:529–534, 2010.

[39] Dierolf M. et all. Ptychographic x-ray computed tomography at the nanoscale. *Nature*, 467:436–439, 2010.

[40] Menzel A. Thibault P. Reconstructing state mixtures from diffraction measurements. *Nature*, 494:68–71, 2013.

[41] Cullis A. Rodenburg J.M., Hurst A. Transmission microscopy witwith lenses for objects of unlimited size. *Ultramicroscopy*, 107:227–231, 2007.

[42] Sweeney F. Midgeley P.A. Rodenburg J.M., Maiden A.M. Wave-front phase retrieval in transmission electron microscopy via ptychography. *Phys Rev B*, 82:121415–, 2010.

[43] Faulkner H.M. Rodenburg J.M. A phase retrieval algorithm for shifting illumination. *Applied Physics Letters*, 85:4795–4797, 2004.

[44] Maiden A.M. Rodenburg J.M. An improved ptychographical phase retrieval algorithm for diffractive imaging. *Ultramicroscopy*, 109:1256–1262, 2009.

[45] Elser V. Phase retrieval by iterated projections. *Journal of the Physics Society of America*, 20:40–55, 2003.

[46] Thibault P. et all. High-resolution scanning x-ray diffraction microscopy. *Science*, 321:379–382, 2008.

[47] Bunk O. Menzel A. Pfeiffer F Thibault P., Dierolf M. Probe retrieval in ptychographic coherent diffractive imaging. *Ultramicroscopy*, 109:338–343, 2009.

[48] Guizar-Sicairos M. Mantion A. Kewish C.M. Menzel A. Bunk O. David C. Vila-Comamala J., Diaz A. Characterization of high-resolution diffractive x-ray optics by ptychographic coherent diffractive imaging. *Optics Express*, 19(22):21333–21344, 2011.

[49] Cole H. Batterman B. W. Dynamical diffraction of x-rays by perfect crystals. *Reviews of Modern Physics*, 36:681–717, 1964.

[50] Vila-Comala J. Diaz A. Berenguer F. Bean R. Chen B. Menzel A. Robinson I.K. Rodenburg J.M. Zhang F., Peterson I. Translation position determination in ptychographic coherent diffraction imaging. *to be submitted for publication.*

[51] Rodenburg J.M. Maiden A.M., Humphry M.J. Ptychographic transmission microscopy in three dimensions using a multi-slice approach. *J. Opt. Soc. Am.*, 29:1606–1614, 2012.

[52] R. J. Sarahan M.C. Kraus B. Rodenburg J.M. Maiden A.M., Humphry M.J. An annealing algorithm to correct positioning errors in ptychography. *Ultramicroscopy*, 120:64–72, 2012.

[53] Martin A.V. Quiney H.M. Allen L.J. D'Alfonso A.J., Morgan A.J. Fast deterministic approach to exit-wave reconstruction. *Phys Rev A*, 85:031816–, 2012.

[54] Kewish C.M. et all. Reconstruction of an astigmatic hard x-ray beam and alignment of k-b mirrors from ptychographic coherent diffraction data. *Optics Express*, 18:23420–23427, 2010.

[55] Thibault P. et all. High-resolution scanning x-ray diffraction microscopy. *Science*, 321:379–382, 2008.

[56] Bravin A. Fernandez M. Tenhunen M. Virkkunen P. Suortti P. Keyrilainen, J. Phase-contrast x-ray imaging of breast. *Acta Radiologica*, 51(8):866–884, 2010.

[57] Bates R.H.T. Rodenburg, J.M. The theory of super-resolution electron microscopy via wigner-distribution deconvolution. *Philosophical Transactions of the Royal Society of London. Series A: Physical and Engineering Sciences*, 339:512–553, 1992.

[58] Hoppe W. *Acta Crystallographica*, 25:495–501, 1969.